Adhesion force spectroscopy with nanostructured colloidal probes reveals nanotopography-dependent early mechanotransductive interactions at the cell membrane level

M. Chighizola, A. Previdi, T. Dini, C. Piazzoni, C. Lenardi, P. Milani, C. Schulte*, A. Podestà*

C.I.Ma.I.Na. and Dipartimento di Fisica "Aldo Pontremoli",
Università degli Studi di Milano, via Celoria 16, 20133 Milan, Italy.

*Corresponding authors:
alessandro.podesta@mi.infn.it; carsten.schulte@unimi.it

ABSTRACT

Mechanosensing, the ability of cells to perceive and interpret the microenvironmental biophysical cues (such as the nanotopography), impacts strongly on cellular behaviour through mechanotransductive processes and signalling. These events are predominantly mediated by integrins, the principal cellular adhesion receptors located at the cell/extracellular matrix (ECM) interface.

Because of the typical piconewton force range and nanometre length scale of mechanotransductive interactions, achieving a detailed understanding of the spatiotemporal dynamics occurring at the cell/microenvironment interface is challenging; sophisticated interdisciplinary methodologies are required. Moreover, an accurate control over the nanotopographical features of the microenvironment is essential, in order to systematically investigate and precisely assess the influence of the different nanotopographical motifs on the mechanotransductive process.

In this framework, we were able to study and quantify the impact of microenvironmental nanotopography on early cellular adhesion events by means of adhesion force spectroscopy based on innovative colloidal probes mimicking the nanotopography of natural ECMs.

These probes provided the opportunity to detect nanotopography-specific modulations of the molecular clutch force loading dynamics and integrin clustering at the level of single binding events, in the critical time window of nascent adhesion formation. Following this approach, we found that the nanotopographical features are responsible for an excessive force loading in single adhesion sites after 20 – 60 s of interaction, causing a drop in the number of adhesion sites. However, by manganese treatment we demonstrated that the availability of activated integrins is a critical regulatory factor for these nanotopography-dependent dynamics.

KEYWORDS

Mechanosensing, mechanotransduction, mechanobiology, cell adhesion, nanotopography, nanostructured materials, cell microenvironment, extracellular matrix, atomic force microscopy, colloidal probes, adhesion force spectroscopy, integrin binding, adhesion complexes.

1. INTRODUCTION

A complex crosstalk between cells and their microenvironment, i.e. the extracellular matrix (ECM), governs the development and maintenance of multicellular tissues. The biophysical properties of the microenvironment were therein identified as critical factors for the regulation of many cellular responses, such as proliferation, migration, and differentiation. The ECM is a complex meshwork of intertwined macromolecules (with protein and sugar components) characterised by the presence of fibrillary and reticular structures, pores and asperities at the nanoscale. The configurations can be relatively ordered, as e.g. in fibrillary collagen-dominated ECM, or instead rather disordered, as in basement membranes or brain ECM. However, on the local nanoscale level often irregularities, anisotropies and density gradients are present[1–6].

In recent years, it became evident that mechanical stimuli of the ECM, such as rigidity and/or spatial organisation and dimensionality of adhesion sites (e.g., in terms of geometry and topography), alter intrinsic cellular properties, such as the actin cytoskeletal organisation/mechanics and the signalling status[7–10]. The intricate processes through which the cell perceives and reacts to mechanical and structural stimuli in its microenvironment were termed mechanosensing and mechanotransduction[11–18].

Mechanotransductive processes are involved in virtually all aspects of the cellular life and tissue organisation[11–19] and aberrations in components that participate to mechanosensing and mechanotransduction have been linked to various diseases, in particular in cancer and metastasis. A detailed comprehension of how biophysical ECM characteristics modulate mechanotransduction would promote new approaches for treatments of diseases, drug therapies or diagnostic approaches, exploiting and targeting identified mechanotransductive key regulators or structures[11,20–26].

Cells sense the biophysical microenvironmental information at the nanoscale, and the nanotopography emerged as a crucial parameter in the regulation of mechanotransductive processes and signalling[7–9,27–31]. The mechanotransductive pathway is primarily mediated by specific transmembrane proteins, called integrins, and modulated by the extent to which these integrins cluster together into integrin adhesion complexes (IACs) and mature into bigger structures, such as focal complexes and focal adhesions (FAs). The extent of integrin clustering and FA maturation, in turn, depends on the force loading within the so-called molecular clutches of nascent adhesions, i.e. the initial connection of the ECM-binding integrins to forces generated by the actin cytoskeleton *via* adaptor proteins (in particular talin and vinculin). The spatial organisation of integrin adhesion sites (ligands) exerts a fundamental influence on the integrin clustering and eventually on cellular behaviour and responses. These effects are mediated in particular through the principal elements of

mechanotransductive signalling, such as RhoGTPases, the actin cytoskeleton and mechanosensitive transcription factors (e.g., YAP)[11–19].

However, a better understanding and quantification of the dynamics in the cell/microenvironment interface and the force development in the early steps of cellular mechanosensing in response to different topographical stimuli is required. In particular, although the presence of nanotopographical disorder (due to the impact on the spatial distribution of integrin ligands) has been shown to have a strong influence on protein adsorption, cell adhesion, integrin clustering and differentiation[7,26,31–33], the systematic characterisation of the influence of disordered configurations with different nanoscale three-dimensional features is still in its infancy.

To unravel the molecular mechanisms of cellular mechanosensing and the mechanotransductive responses it provokes in the cells, versatile biophysical approaches are essential[10,17,30,34–42]. Smart biomaterials with complex structural architectures and/or tuneable physical properties are needed to create controllable cellular microenvironments that mimic the *in vivo* ECM situation[30,31,34,36,37,41]. In addition, sophisticated techniques are required that enable the mapping of mechanobiologically relevant alterations in cells[17,35,38,42].

In this context, atomic force microscopy (AFM) represents a powerful tool due to its capacity to allow an accurate probing of cell surfaces, determining cellular mechanical properties[42–46] (and mechanotransduction-related alterations[47–49]), and measuring adhesion forces down to the single-molecule contribution[38]. The standard techniques used to test the cellular adhesion properties are Single-Molecule Force Spectroscopy (SMFS)[50] and Single-Cell Force Spectroscopy (SCFS)[51,52]. SMFS consists in a functionalisation of the AFM probe (e.g., coating with ECM proteins) in order to permit the interaction with specific transmembrane proteins. SCFS instead uses the cell itself as a probe (attached to the cantilever) that interacts with the substrates of interest (including other cells).

SCFS has been widely used to study in detail the cooperative action of integrins in early cellular adhesion to fibronectin or collagen[53–55] and their connection to internal cellular biochemical signalling[56]. This technique has furthermore been exploited to test the biocompatibility of materials for implants in orthopaedic surgery[57], or the role of ligand spacing in the cell adhesion using substrates decorated with suitably functionalised nanoparticles, separating integrin ligands with different specific distances[58,59]. A limitation of SCFS, as explained in detail by Naganuma[60], is that the actual contact area between the cell and the substrates cannot be measured. As a matter of fact, the cell, once captured and immobilised on the tipless cantilever, will evolve its own adhesion on the probe itself, changing its morphology during time and with it the adhesion properties. These dynamics will introduce a bias in the force spectroscopy experiment and, since different cells behave differently, make results less comparable between each other.

To address these issues, we propose a reversal of the conventional SCFS approach. Our novel strategy for the study of early mechanotransductive interactions at the cell membrane level is based on the use of functionalised colloidal probes (CPs) mimicking the peculiar nanoscale topographical features of *in vivo* ECM for force spectroscopy experiments on living cells. The probes represent the source for the mechanical cues regulating the cascade of the mechanotransductive events. By inverting the typical cell-microenvironment interaction geometry (Figure 1), we take in particular control over the cell/substrate contact area and obtain a more accurate assessment of the forces and molecular interactions that develop at the cell membrane during the early mechanotransductive events.

Our technological approach for the fabrication of nanotopographical surfaces consists in growing a cluster-assembled thin film of nanostructured zirconium oxide (ns-ZrO_2, zirconia) with disordered, yet controlled, topographical features by means of supersonic cluster beam deposition (SCBD)[61–63]. Zirconia is a biocompatible material used in various clinical applications, particularly for its chemical inertness and structural properties[64]. SCBD is an additive technique and the disordered surface morphology of the deposited films is characterised by nanoscale roughness and other morphological parameters, like the surface area or the correlation length, which can be accurately tuned and reproduced by controlling the film thickness through the deposition time[65].

The obtained disordered nanostructured films possess nanotopographical features that resemble those that can be observed in *in vivo* ECM (e.g. in basement membranes or in the brain[5,6]) and with nano-3D configurations (in terms of asperity dimensionality and distances) that have a potential to modulate integrin-dependent mechanotransductive processes and signalling[32,47,61,66–70] (Figure 1a). Indeed, also in those ECMs whose structure is dominated by fibrillar features, there are often irregularities at the nanoscale, e.g. in regards to distances and heights of fibres or in the pore sizes of reticular, crosslinked structures, which are well represented by the nanotopographical features of the ns-ZrO_2[6,47].

Using these nanostructured thin films as substrates (Figure 1a), we have recently shown that the interaction of cells, in particular neuronal cells, with the nanotopographical features, impacts decisively on mechanotransductively relevant events, such as FA maturation, cytoskeletal organisation/mechanics and integrin signalling, as well as the cellular program and differentiative behaviour[47,61,66,67,71].

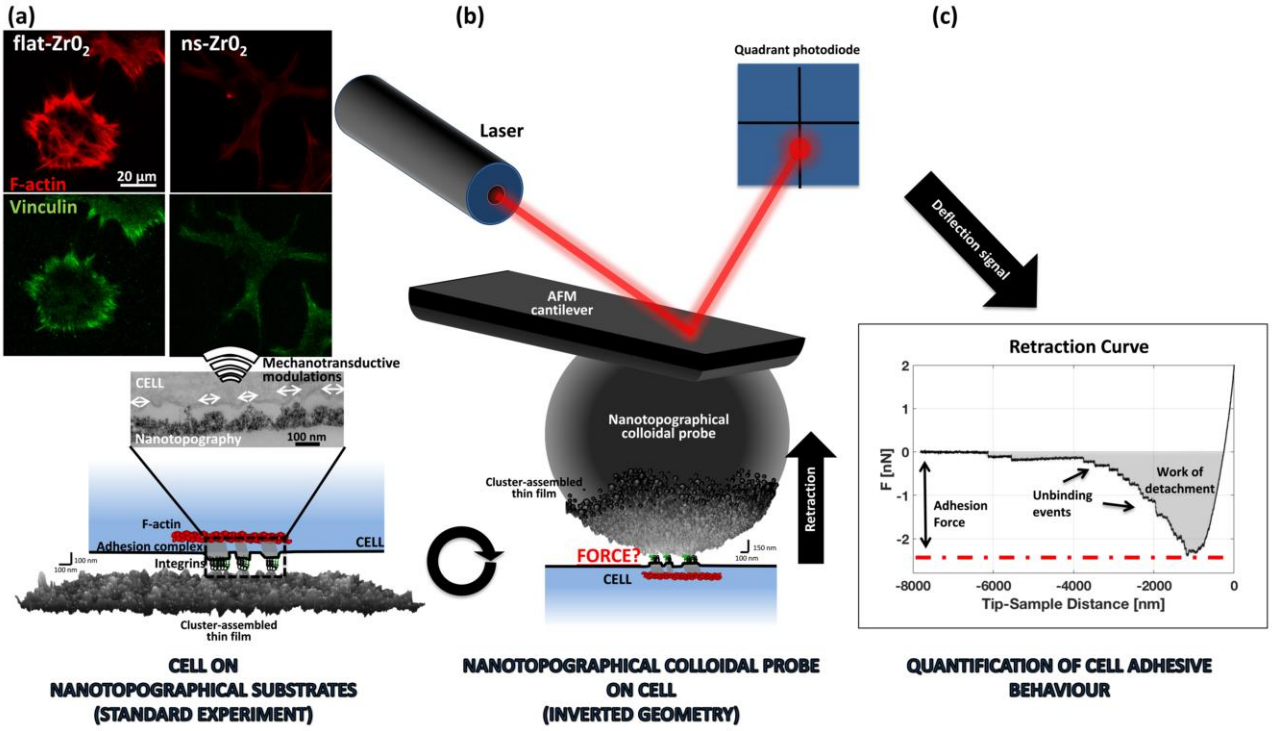

Figure 1 – Approach of adhesion force spectroscopy by means of colloidal probes functionalised with extracellular matrix-mimicking nanotopographical features. ***(a)*** *The scheme at the bottom left illustrates the conventional approach used to study the impact of nanotopographical features on mechanotransductive processes. The image inset shows a transmission electron microscopy (TEM) image of an interaction sites between a PC12 cell and the asperities of cluster-assembled ECM-mimicking nanotopographical zirconia substrate (indicated by the white arrows) with an rms roughness r_q = 15 nm (ns-ZrO_2), for which we have shown that it induces mechanotransductive modulations*[47]*. The immunofluorescence (IF) images in the panel above (in green, total internal reflection recordings of vinculin staining; in red, epifluorescence recordings of the actin filaments marked by phalloidin staining) demonstrate that, after 4 hours of interaction on the nanotopographical ns-ZrO_2 substrate, only small punctate focal complex size adhesion sites formed and stress fibres were absent, whereas on the flat zirconia (flat-ZrO_2), focal adhesions and stress fibres are present*[47]*. TEM and IF images were adapted from Schulte et al.*[47]*.* ***(b)*** *Schematic illustration of the approach to measure adhesion forces to colloidal probes with a nanotopographical surface (r_q = 15 nm) produced by SCBD (the scale bars close to the nanostructured surfaces refer only to the nanotopography, other graphical icons are symbolic and not in scale).* ***(b,c)*** *Examples of the deflection signal extracted with the AFM and used to quantify the cellular adhesive behaviour in response to different nanotopographies.*

Instead of plating the cells on the nanostructured substrates, here we exploited the nanotopographical colloidal probes (nt-CPs) to stimulate the cells and to characterise the interfacial integrin adhesion dynamics by means of adhesion force spectroscopy (Figure 1b). Compared to our previous experiments, this approach provided access to phenomena that occur at the cell-microenvironment interface that would otherwise be buried below the cell body.

To date, only few protocols have been developed to functionalise AFM probe surfaces either with ECM proteins, like collagens, laminins, or cellulose nanofibers[72,73] or with nanoparticles[74–76]. In the former case, natural biomaterials were typically deposited onto CPs, but poor or null control over the nanoscale topography was possible. In the latter case, AFM standard sharp tips were decorated with nanoparticles in order to study their interaction with cells; in other experiments the AFM tip apex was used to model a single nanoparticle[77]. Our nt-CPs were instead used to study the early steps of the cell adhesion to an ECM-mimicking nanotopography with the sensitivity of adhesion force spectroscopy measurements. Following this innovative approach, we were able to follow the temporal evolution of early integrin-related adhesion events at the interface between the cell and a nanotopographical microenvironment at the level of single adhesion events and piconewton force range. To our best knowledge, in this framework of cell/nanotopography interaction such a resolution has not been achieved to date.

2. RESULTS AND DISCUSSION

2.1 Characterisation of the nanotopographical colloidal probes

Figure 2 shows representative AFM images of a clean borosilicate glass sphere before (Figure 2a) and of the same sphere after deposition of the ns-ZrO_2 film (Figure 2b) used for the production of a nt-CP (Fig. S1).

Ns-ZrO_2 grows on the curved CP surface, as it does on conventional flat smooth substrates (see Supplementary Information for details, Fig. S2).

The structure and morphology of these cluster-assembled films result from the random stacking and aggregation of impinging nanometer-sized building blocks (the ZrO_2 clusters) into larger and larger units. The surface profiles of nanostructured zirconia films are characterised by peaks and valleys (see Figure 2c), defining a complex random pattern of nanoscale features, whose dimensions and spatial distribution resemble those found in natural ECM topographies[5,6]. The specific surface area, the rms roughness, the average lateral dimensions of the largest morphological features (the correlation length ξ), as well as the interfacial porosity of the films typically increase with film thickness[62,63,78]. The interfacial open pores, delimited and defined by the surface asperities[47], can

accommodate proteins (including fibronectin and vitronectin, which are present in the serum supplement of the culture medium we used) and nutrients[33,78–81] ; asperities evolve in height, area, and surface charge density[82].

In this work, we concentrated our attention on nt-CPs with rms roughness of the ns-ZrO_2 film r_q = 15 nm. This particular value of r_q was chosen because we recently demonstrated that it induces in PC12 cells mechanotransductive modulations at the level of integrin adhesion complexes and cytoskeleton (Figure 1a), as well as differentiative events, such as neuritogenesis, and a vast change in the cellular program[47,61,67].

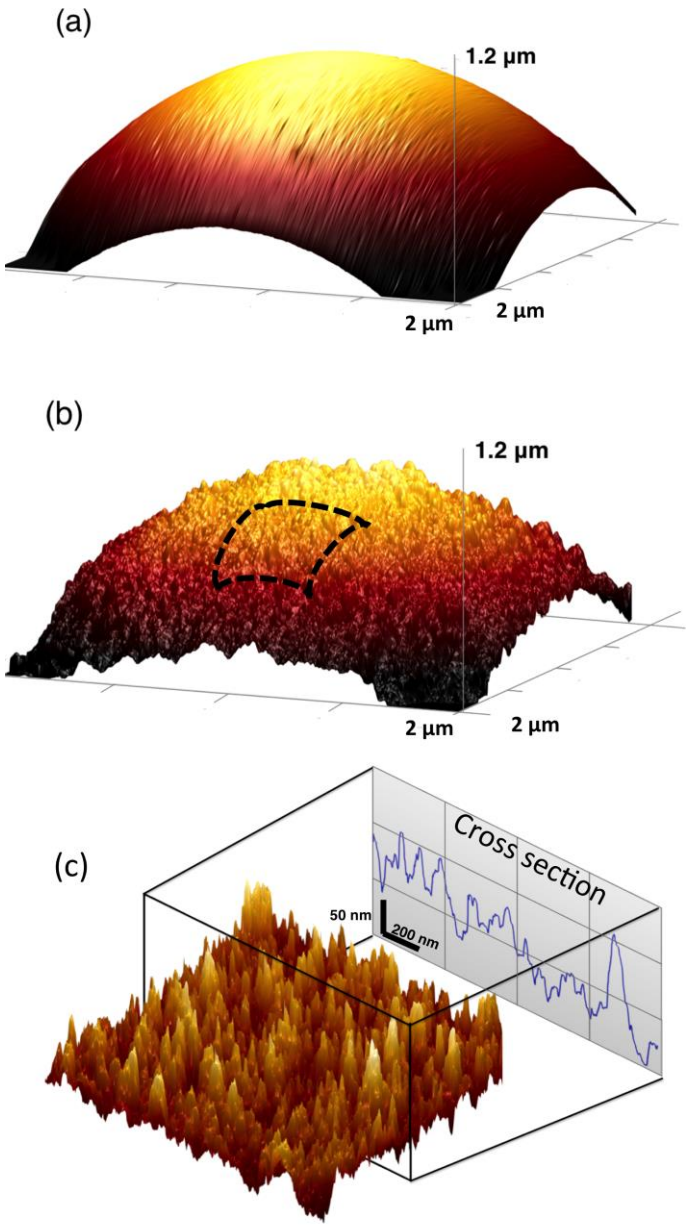

Figure 2 – Comparison of the surface morphology of the colloidal glass probes before and after the deposition of the zirconia nanoclusters. *The surface morphology characterised by AFM of a borosilicate glass sphere.* ***(a)*** *Before, and* ***(b)*** *after the deposition of ns-ZrO_2 (r_q = 15 nm).* ***(c)*** *A higher resolution AFM image (the baseline curvature was removed) from the nt-CP shown in (b); the cross section highlights distinct peaks and valleys at the nanoscale.*

2.2 Cell adhesion dynamics at nanotopographical interfaces

To investigate in which way nanotopographical features influence the characteristics of cellular adhesion processes, we performed adhesion force spectroscopy on PC12 cells with four CPs, possessing different types of functionalisation:

1) ns-ZrO_2 –coated CP, produced by SCBD, with r_q = 15 nm (surface: ns-ZrO_2).

2) flat ZrO_2 –coated CP, produced by ion gun sputtering, without nanotopographical features, r_q < 1 nm (surface: flat-ZrO_2).

3) borosilicate glass CP (surface: glass).

4) poly-L-lysine –coated CP (surface: PLL).

The choice of the PC12 cells as cellular system and these surface conditions was based on our previous work, where we found that the PC12 cells formed FA and stress fibres on the PLL-coated glass and flat zirconia substrates, whereas on the ns-ZrO_2 (r_q = 15nm) substrate the adhesion sites remained at focal complex dimensions and the stress fibre formation was reduced[47] (Figure 1a). PLL coatings represent the canonical substrate condition for PC12 cell experimentation, and are also routinely used to facilitate protein absorption and cell adhesion to solid surfaces (in particular glass) in biological applications (by providing positively charged sites favouring electrostatic interactions). The untreated glass CP instead served as a (negative) control because PC12 cells adhere scarcely to nude glass.

The dependence on the contact time *ct* of the measured parameters (maximum adhesion force, work of detachment, number of unbinding events for jumps and tethers, see Figure S4) is discussed in the next paragraphs.

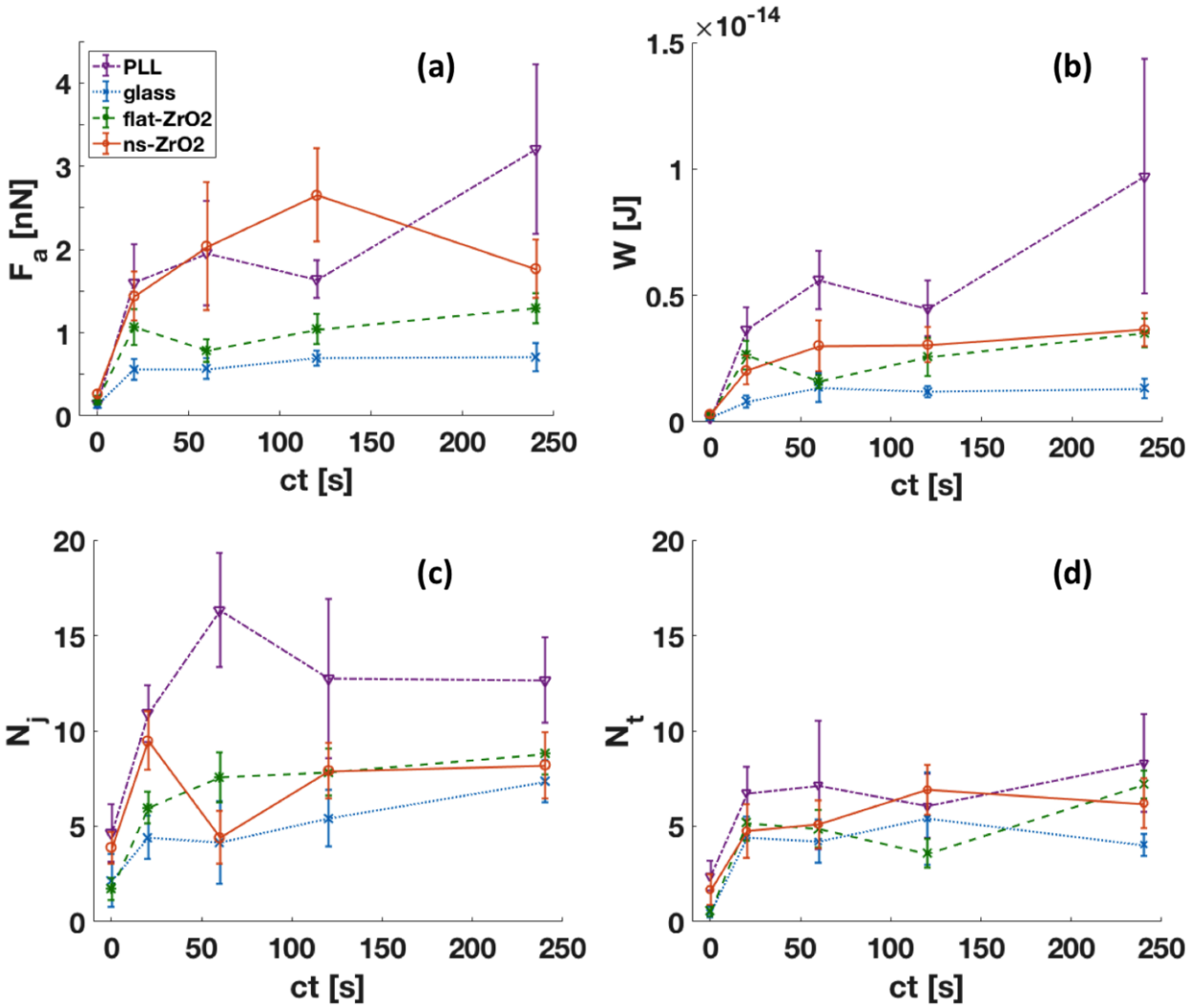

Figure 3 – The nanotopographical features provoke specific effects on the adhesion dynamics, in particular with respect to jump events. *The panel shows the results of the adhesion spectroscopy measurements performed with the four different probe surface conditions: untreated (glass, blue line) or with PLL functionalisation (PLL, violet line), zirconia films, flat (flat-ZrO_2, green line) or with nanotopographical features with a roughness r_q = 15 nm (ns-ZrO_2, orange line). Four different parameters were extracted from the force curves (see Figure 1c and Figure S4) which have been analysed for 5 different cell/probe contact times (ct = 0 s, 20 s, 60 s, 120 s and 240 s), i.e. the maximum adhesion force (F_a), work of detachment (W), mean number of unbinding events, identified as jumps (N_j) or tethers (N_t) (for details see Fig. S4).* ***(a)*** *Dependence of the adhesion force F_a and* ***(b)*** *work W on the contact time. F_a of PLL and ns-ZrO_2 are significantly higher ($p < 0.05$) than glass for all cts (except 0 s) and higher than flat-ZrO_2 at 60 s (ns-ZrO_2 also at 120 s); flat-ZrO2 > glass at 20 s, 120s, and 240 s ($p < 0.05$).W of PLL is higher than glass at 120 s and 240 s ($p < 0.05$).* ***(c)*** *N_j counted per contact time; N_j for PLL is higher than ns-ZrO_2 and flat-ZrO_2 at 20 s, 60 s and 240 s ($p < 0.05$), at 20 s ns-ZrO_2 is higher than flat-ZrO_2 ($p < 0.05$), and Nj of ns-ZrO_2 at 20 s is higher than*

*at 60 s ($p < 0.05$). **(d)** Mean number of tethers per contact times. The error bars represent effective standard deviations of the mean (details in the Supplementary Information).*

Maximum adhesion force F_a. Figure 3a shows that the cells are capable to create stronger adhesion on all functionalised surfaces, compared to the untreated glass (PLL vs glass, $p < 0.05$, except 0 s; ns-ZrO_2 vs glass, $p < 0.05$, except 0 s; flat-ZrO_2 vs glass, $p < 0.05$, except 0 s and 60 s). Nevertheless, the extent of these differences compared to the reference glass surface, and the temporal evolution of the adhesion, are different on each surface.

On glass and flat zirconia, F_a rapidly reaches a plateau, although on flat-ZrO_2 the final value is higher. On ns-ZrO_2 and PLL, F_a follows a similar growing trend in the first 60 s, reaching much higher values than flat-ZrO_2 (both $p < 0.05$). PLL is the only surface where adhesion increases during the whole time interval, achieving its maximum values at 240 s (with the highest value of all the conditions). On the nanotopographical surface, the F_a maximum is reached at 120 s, then adhesion decreases to a value similar to that on flat-ZrO_2.

Work of Detachment W. The temporal evolution of the work of detachment W provides additional information about the level of complexity and the maturation of the cellular adhesion (Figure 3b). While the trends of W for glass and PLL-coated glass are similar to those of F_a *(significantly higher at 120 s and 240 s, $p < 0.05$)*, this is not the case for zirconia surfaces; while the evolution of F_a was different for the two zirconia surfaces, the evolution of W is similar. Moreover, the measured work for both flat-ZrO_2 and ns-ZrO_2 never reaches the value of the PLL-coated glass. Since the work is a force times a distance, a different trend of W compared to F_a can be attributed to either different numbers of bonds (detected as unbinding events), or to different bond lengths, or both.

Mean number of unbinding events N_j, N_t. The mean number of detected unbinding events for cells interacting with different surfaces (Figure 3c-d) revealed distinct differences in the temporal adhesion dynamics between PLL, ns-ZrO_2 and flat-ZrO_2, in particular with respect to the jump events N_j, which we discuss first (Figure 3c).

The jump events in force curves are predominantly attributed to receptors in the membrane that are anchored to the cytoskeleton (as e.g. integrins in molecular clutches via talin)[51,54–57,83–85].

PLL-coated glass (Figure 3c) and ns-ZrO_2 show a similar progression of the N_j in the first 20 s (with both reaching 10 events), after which they develop differently. The difference between the ns-ZrO_2 and the flat-ZrO_2 condition is significant at 20 s ($p < 0.05$). The N_j of PLL reaches a maximum at 60 s, and also later on the cells created significantly more jump adhesion spots on the PLL compared to flat-ZrO_2 and ns-ZrO_2 ($p < 0.05$ at 60 s and 240 s).

In the nanotopographical surface condition, N_j decreases strongly (-53%) from 20 s to 60 s ($p < 0.05$). Intriguingly, this drop is a recurrent and specific phenomenon that appears systematically for all investigated cells interacting with the nanotopographical surface. In the flat-ZrO_2 condition, there is instead a progressive rise of N_j in the first 120 s (reaching 8 events).

The evolution of the number of tethers N_t (Figure 3d) instead is more similar for all four conditions.

The nature of the tethers has been poorly investigated, but they are usually associated to receptors that are not anchored to the internal actin cortex, which results in membrane extrusion from the cell reservoir[83–85]. Another hypothesis is that tether events could, at least partially, be related to the unfolding of glycocalyx sugar chains[86]. It has been demonstrated that the tethers do not respond as a catch bond[55], and also in our experimental set-up they seem to participate in a negligible manner to the maturation of the adhesion (with a generally low contribution to F_a, see Supplementary Information, Figure S6), showing only minor divergent reactions towards the different surface conditions.

In the following, we will concentrate our attention mainly on the N_j parameter.

The interaction time window between 20 and 120 s seems to be the most interesting for the dynamics of the adhesion spots on different surfaces, in particular when looking at the combined evolution of the different parameters (e.g., F_a and N_j).

PLL and ns-ZrO_2 have a comparable development of F_a from 20 to 60 s, whereas the N_j evolve in a converse manner, i.e. it increases markedly for PLL, and decreases for the nanotopographical surface (Figure 3a,c). Glass and flat-ZrO_2 instead show more moderate alterations.

In order to better investigate these dynamical phenomena, we have calculated the mean adhesion force per jump $\langle F_j \rangle$ (see Supplementary Information for details, Figure S6). The result is shown in Figure 4. An interesting outcome specific for the ns-ZrO_2 surface is visible. While the average force per single jump (between 20 - 120 s) is similar for all the surfaces without nanotopographical features, i.e. glass, PLL, and flat-ZrO_2, a sudden 3.3-fold increase of the single jump strength ($p < 0.05$ for ns-ZrO_2 20 s vs 60 s; $p < 0.05$ for the comparison between flat-ZrO_2 and ns-ZrO_2 at 60 s and 120 s) is evident for ns-ZrO_2. At regime, after 240 s, the force $\langle F_j \rangle$ converges down to the value of the other surfaces, nevertheless it remains significantly higher compared to glass and flat-ZrO_2 for most of the time.

Interestingly, these divergent dynamics happen in the critical time window for molecular clutch reinforcement, the initiation of integrin clustering and nascent adhesion growth[55,87].

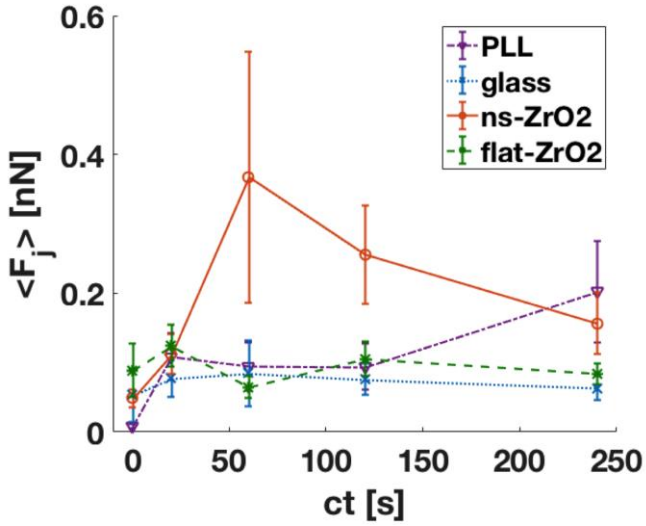

Figure 4 – Nanotopography-specific increase in jump adhesion force loading. *The graph shows the evolution of the mean jump force <F_j> in dependence of the contact times for the different probe surfaces (glass: blue line; PLL: violet line; flat-ZrO_2, green line; ns-ZrO_2, orange line; the difference between ns-ZrO_2 20 s vs 60s is significant ($p < 0.05$) and ns-ZrO_2 is higher than the other surfaces at 60 s and 120 s ($p < 0.05$). The specifics of the <F_j> calculation can be found in the Supplementary Information (Figure S6). The error bars represent effective standard deviations of the mean (details in the Supplementary Information).*

2.3 Adhesion dynamics to the nanotopographical probe are influenced by the availability of activated integrin and depend, at least partially, on β1 integrin

Due to our previous data on the effects of the nanotopography on the configuration of integrin adhesion sites[47] and the interesting chronology of the jump adhesion events and force development observed for the ns-ZrO_2 surface, we tested in which way these dynamics towards the nanotopography depend on the integrin activity.

In a first step, we examined how an excess of integrin activation would affect the early adhesion dynamics towards the nanotopographical surface. To this purpose, we activated the integrins with Mn^{2+}. This treatment kept the N_j from dropping after 60 s ($p < 0.05$), as it was observed on the ns-ZrO_2 surface without Mn^{2+} activation (Figure 5a).

This impact of the abundant availability of activated integrins might be explained by two effects (or a combination of both). In nascent adhesions, Mn^{2+}-induced integrin activation is known to increase the density within integrin clusters[88]; moreover, unligated activated integrins could favour the bridging between separated, but adjacent adhesion sites[89]. In any case, the force loading can be

distributed over more active integrins, confirmed by the decrease of mean force per jump event at 60 s due to the Mn^{2+} treatment (Figure 5b, $p < 0.05$ for 60 s), which stabilises the adhesion sites.

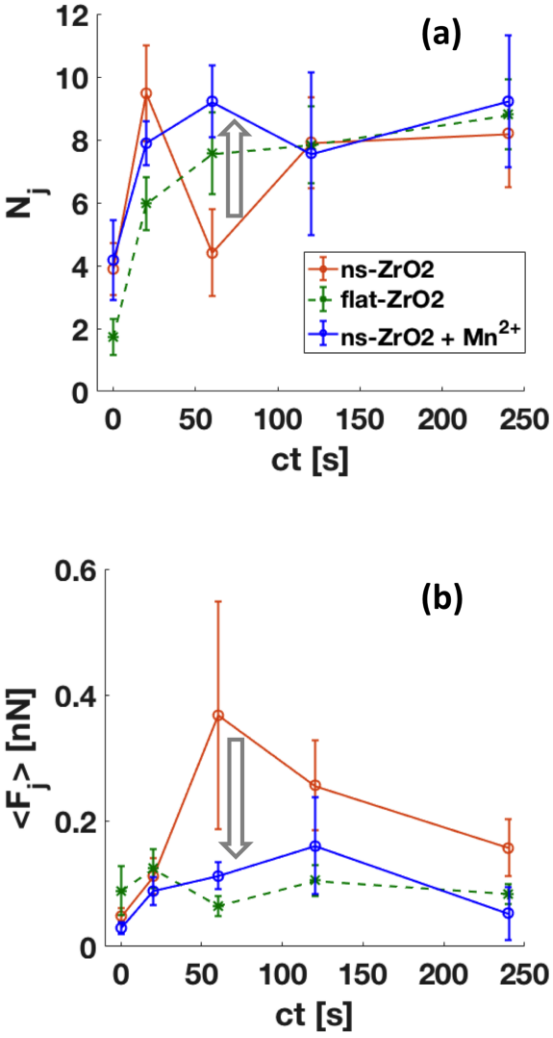

Figure* 5 – Mn^{2+}-induced global integrin activation averts nanotopography-specific drop in jump events and excessive force loading.** *The graphs demonstrate the* ***(a) *mean number of jumps N_j detected on ns-ZrO_2 surface before (orange) and after (blue) Mn^{2+} treatment (1 mM for >10 min to obtain global integrin activation) versus the contact time, and the* ***(b)*** *mean jump force $<F_j>$ measured on ns-ZrO_2 before (orange) and after (blue) Mn^{2+} treatment versus the contact time. The flat-ZrO_2 values (green, reproduced from Figure 7) are also shown for sake of comparison. After the Mn^{2+} treatment, N_j was higher and $<F_j>$ was lower at 60 s (both $p < 0.05$) in the ns-ZrO_2 condition, highlighted by the grey arrows. The error bars represent effective standard deviations of the mean (details in the Supplementary Information).*

Furthermore, we treated the cells with an allosteric inhibitory antibody against β1 integrin (4b4), to see how this would impact on N_j. As shown in Figure 6, in the presence of the 4b4, N_j

decreased at all contact times (from 36% (*ct* = 60 s) to 60% (*ct* = 240 s), $p < 0.05$ for all *cts)*. Since β1 integrin represents the most common, but not the only, β integrin subunit, this result demonstrates that the recorded jump interaction events depend, at least partially, on the activation of β1 integrin subunit-containing integrin receptors. This outcome is in line with the involvement of the (β1) integrin activation and signalling in the nanotopography-sensitive modulations in PC12 cell mechanotransduction and differentiative behaviour (in particular neuritogenesis) we have previously reported[47,67].

Altogether, these results indicate that the availability of activated integrins seems to be an influential regulatory factor for spatial sensing of adhesion sites at the nanoscale.

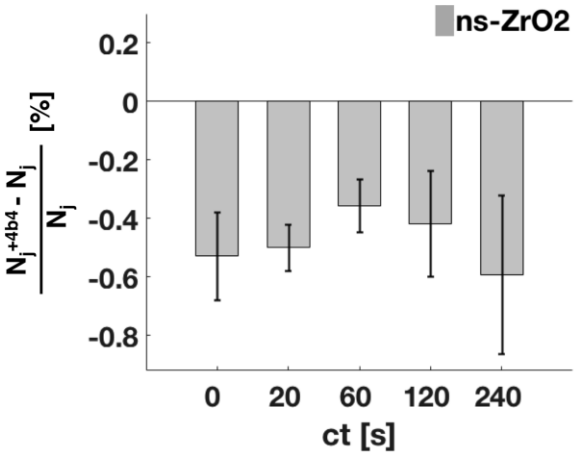

Figure 6 – Inhibition of β1 subunit-containing integrins strongly reduces the number of jump events. *The graph shows the relative change [%] of mean number of jumps N_j in the ns-ZrO_2 condition after the 4b4 antibody treatment (5µg/mL) compared to the untreated ns-ZrO_2. All changes are significant ($p < 0.05$). The error bars represent effective standard deviations of the mean (details in the Supplementary Information).*

These results provide new open questions in regard to nanotopography mechanosensing to be addressed in the future. It has been shown that the interaction of distinct integrin types with ECM ligands contribute differently, and in a force-dependent manner, to mechanotransduction[90–95]. Albeit the inhibition of the β1 integrin subunit covers a variety of ligand specificities, further experiments (e.g. with other inhibitory integrin antibodies or RGD peptides) are needed to dissect more precisely how integrins with different ligand affinities are involved in nanotopography mechanosensing. In

addition, the nt-CPs were not functionalised with a specific ECM ligand (the same is true for the substrates used in our previous experiments with PC12 cells[47,61,67]), but due to the presence of serum in the medium, e.g. fibronectin and vitronectin can adsorb to the probe surfaces (the >30 min pre-incubation of the probes with the medium before starting the measurements was done exactly for this reason). It will be important to study in the future (by coating the probes e.g. with RGD peptides, laminins, fibronectin, vitronectin, or collagens) in more detail how specific ECM ligands modulate the adhesion dynamics in dependency of the topography. These combined experiments will lead to a better understanding of the contribution of different integrin types and ECM ligands to nanotopography-dependent mechanotransduction, and how force loading dynamics is involved in this.

2.4 Evolution of jump force distribution over time.

For a better understanding of the dynamics of the adhesion force development on the different surfaces, we analysed in greater detail the distribution of the measured strengths of the single jumps at different contact time *ct*.

Surfaces	**Most probable jump force at ct = 0 (pN)**
flat-ZrO_2	42±15
ns-ZrO_2	36±13
glass	21±10
PLL	19±17

Table 1. *Most probable jump force at ct = 0s.*

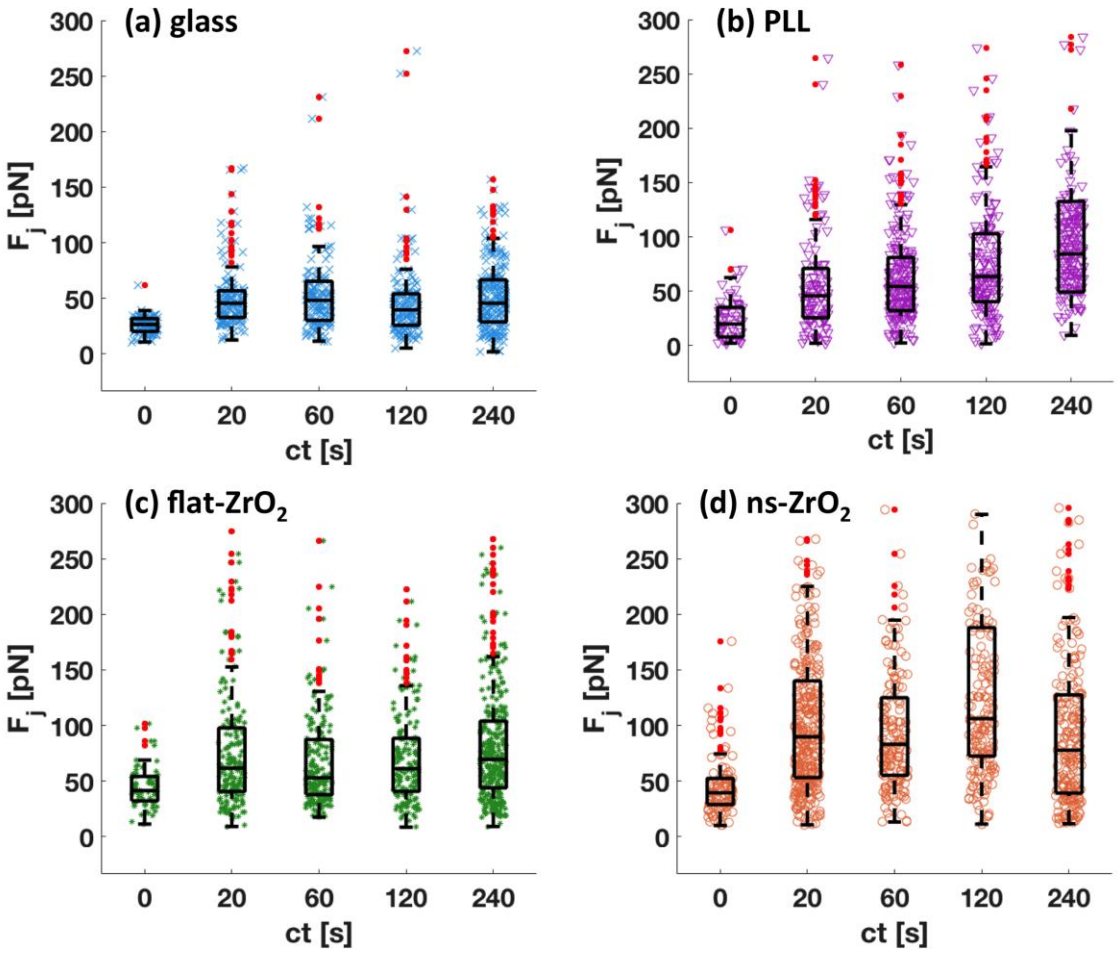

Figure 7 – Early and persistent occurrence of high jump forces specific for the nanotopography condition. *This panel plots the evolution of the distribution of the forces of the single jump events (symbols) for the different contact times for* ***(a)*** *glass (blue),* ***(b)*** *PLL (violet),* ***(c)*** *flat-ZrO_2 (green bars) and* ***(d)*** *ns-ZrO_2 (orange). The boxes indicate the inter-quartile range (with the base representing the first and the top the third quartile, respectively), the lines in the boxes show the median, and the dashed lines highlight the highest and lowest values (red dots mark the outliers).*

At *ct* = 0 s, the distributions of jump forces are similar for all surfaces, with a median value detected around 40 pN for zirconia surfaces and 20 pN for glass and PLL (see Table 1). The immediate appearance of a force in this range is consistent with the recently shown very fast integrin adhesion response (in that case for α5β1 integrin/fibronectin binding)[53]. The range is also compatible with the reported peak tension of single integrin-ligand bonds during initial adhesion[54,96–100] and furthermore, it coincides with the force thresholds for the extension of the talin rod, vinculin recruitment and molecular clutch reinforcement[101].

With the increase of *ct*, we observed that on glass the median jump force remains almost constant, with the appearance of few events at higher forces around 120 pN (Figure 7a). On PLL (Figure 7b), a constant increase of the jumps forces can be noted, even if the lower force values (around 20 pN) remains always present. The distribution of flat-ZrO_2 (Figure 7c) is similar, although the events are more scattered and there are more counts at higher forces at small contact times.

On ns-ZrO_2 (Figure 7d), the distribution of forces, already after 20 s, shifts towards higher forces, even above 200 pN. High force bonds (>100 pN) appear almost with the same frequency (~45%) as the weaker ones (<100 pN) at every contact time (0 s excluded).

Regarding the adhesion force F_a (Figure 3a), this increased strength of the single jumps actually compensates for the lower number of adhesion spots compared to the PLL-coated glass (in particular at *ct* = 60 s, see Figure 3c). In other words, on the nanotopographical surfaces the adhesion spots are exposed to higher forces. The decrease of high-force unbinding events on ns-ZrO_2 observed at *ct* = 240 s, with respect to earlier *cts*, is compatible with the general decrease of the F_a (Figure 3a).

We point out how the increased occurrence of higher-force events (Figure 4 and 7) happens simultaneously with the drop of N_j (Figure 3c), which depend on the availability of activated integrins (Figure 5), in the ns-ZrO_2 condition. This is peculiar, in particular because it happens during the critical time window for nascent adhesion growth and integrin clustering[87]. These complex nanotopography-specific adhesion dynamics are not explainable by increased protein adsorption because of the higher roughness of the nanostructured surface (as reported in Scopelliti et al.[80] and Gailite et al.[79], partially due to the increase in surface area and nanoporosity). If ligand adsorption were the decisive factor, we would expect for the flat-ZrO_2 versus ns-ZrO_2 comparison similar dynamics as we have observed for the glass +/-PLL situation. The observed temporal course of the nanotopography-specific adhesion dynamics could rather indicate that too small and/or too separated adhesion sites (critical thresholds for integrin clustering have been determined to be ≥60-70 nm) disintegrate, due to exposure to excessively high forces. Instead, when the conditions are suitable, bigger clusters of integrin form and succeed to reinforce and mature[58,59,68–70] (Figure 8). These clusters might need to exceed at least the size of the minimal adhesion unit of a few integrins in sufficiently close, i.e. tens of nanometres, vicinity[89,102]; which is consistent with the appearance of the second peak at 120 pN.

These results are compatible with the dimensions of the nanotopographical features and the confinement action at the nanoscale, provided by the small contact area offered by the asperities of the nanostructures and the distance between them.

We have demonstrated previously that the PC12 cells are in contact only with the apical part of the nanotopographical asperities, which restricts the size of the adhesion sites to the nanometric

level, and inhibits the maturation of bigger adhesion structures on a larger scale (see Figure 1a). Analyses of TEM images (an example in Figure 1a) showed that the contact areas between the cells and the asperities of the nanotopography (with r_q = 15 nm) have an average width of 53.2 ±48.0 nm (median: 40.4 ±21.6 nm). Moreover, the distances (mean: 99.1 ±101.4 nm, median: 60.4 ±30.4 nm) between the asperities of the disordered nanotopography effectively oscillate around the critical ligand spacing threshold (≥60-70 nm)[47]. The results reported in this work are consistent with these previous observations, and confirm, at the level of single binding events and at the pN scale, the crucial role of force loading in the molecular clutches in the nascent adhesions to accomplish nanometric spatial sensing of adhesion sites, reported recently by Oria et al.[19].

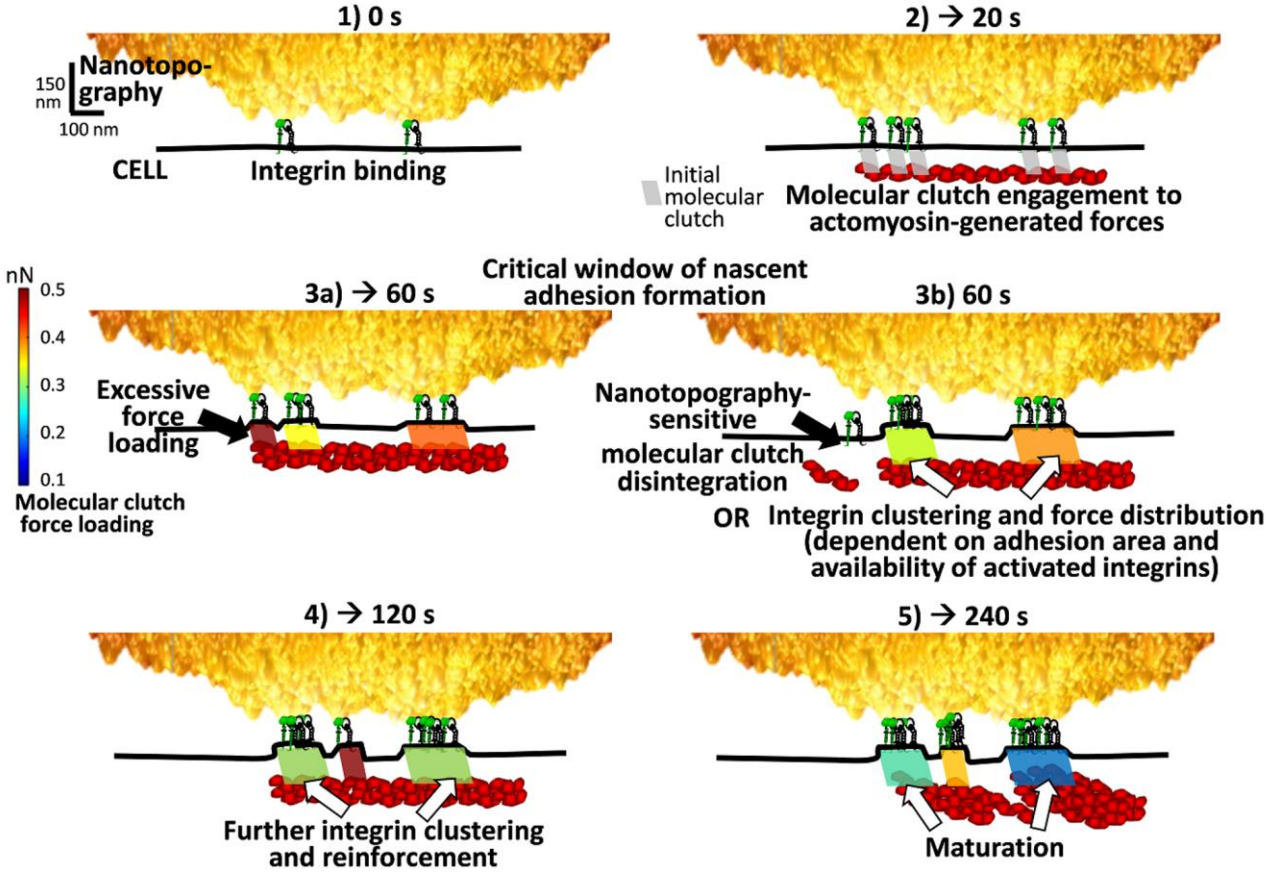

Figure 8 – Suggested mechanism (integrating the experimental results) of nanotopography-dependent adhesion site disintegration, due to excessive force loading, or reinforcement by integrin clustering and force distribution. *These graphics are a visual representation of our actual experimental data integrated into a potential mechanism of nanotopography-sensitive force loading dynamics and consequential adhesion site disintegration or reinforcement. 1) After the almost immediate binding of integrins (0 s contact time), 2) the molecular clutches engage to the actomyosin-generated forces (→ 20 s). 3a) This leads to increasing force loading within the molecular clutches*

(20 – 60 s) in the critical window of nascent adhesion formation. 3b) Depending on the nanotopographical conditions (i.e. existing adhesion area and distance to other adhesion sites) and the availability of active integrins (see Mn^{2+} treatment, Figure 5), either adhesion site disintegration (excessive force loading because of insufficient integrin clustering, black arrows) or reinforcement (integrin clustering and force distribution, white arrows) are induced around 60s. 4,5) Where the nanotopographical conditions are suitable the adhesion sites are sustained further on and mature (white arrows). The colours of the parallelogram icons (symbolising the force loading within molecular clutches due to the engagement of the integrins and the actomyosin-generated forces) code for the force intensities measured by means of our approach at the different contact times (see the colour bar on the left of the middle row, compare values with Figure 4). In the schemes decisive events are highlighted, such as integrin binding, the molecular clutch engagement to actomyosin-generated forces, integrin recruitment/clustering, force distribution, and integrin adhesion complex (IAC) reinforcement/maturation. The length scales on the top left refer to the morphology of the nt-CP only; the other graphical objects (such as the integrins) are not in scale and also their number is symbolic to visualise the development.

3. MATERIALS AND METHODS

3.1 Fabrication and calibration of the colloidal probes

Fabrication of the colloidal probe. The procedure for the fabrication of colloidal probes is based on the approach described in detail in Ref.[103]. Borosilicate glass spheres (Thermo Fisher Scientific), with radius R = 10 ± 1 μm, are first cleaned to remove surface contaminants. The cleaning procedure consists in three sequential 60 seconds centrifugations (10.000 rpm) in a 1:1 water and ethanol solutions, carefully replacing the old with new solution after each centrifugation. The cleaned spheres are then dispersed in toluene and deposited on a microscopy glass slide coated with a thin Au film (with thickness 100 nm) deposited by sputtering. The Au film is used to reduce the capillary force between the sphere and the substrates with respect to that between the sphere and a tipless cantilever[103] (Micromash HQ:CSC38/tipless/no Al, force constant k = 0.02 - 0.03 N/m). The capture of the sphere by the cantilever is done using the XY motorised stage of the AFM microscope, integrated in the optical inverted microscope. The probe is then transferred in a pre-heated high-temperature oven and kept for 2 hours at 780°C. This temperature is slightly below the softening point of borosilicate glass, which is qualitatively defined as the temperature at which a solid object begins collapsing under its own weight. After two hours, the microsphere is covalently attached to the cantilever. Due to the monolithic character of the resulting CP, any gold residue, as well as other

contaminants, can be effectively removed by washing the probe in aqua regia (a mixture of nitric and hydrochloric acids, in a molar ratio of 1:3), or any other aggressive solution.

Determination of the probe radius. The characterisation of the CP radius is performed by AFM reverse imaging of the probe on a spiked grating (TGT1, Tips Nano), as detailed in Ref.[103]. Upon scanning the CP on the spiked grating, hundreds of independent replicas of the probe apical region are obtained. From the measured geometrical properties (like the volume V and the height h) it is possible to determine the value of the radius R by fitting a spherical cap model $V = \frac{\pi}{3}h^2(3R - h)$ to the data. The evaluated probe radius has an accuracy as good as 1%.

Calibration of the cantilever spring constant. The spring constant is calibrated using the thermal noise method[104,105] where a special correction factor is applied in order to take into account the relevant dimension and mass of the glass sphere[106]. For large CPs, the conditions that both dimension and mass of the sphere are small compared to length and mass of the cantilever are not always satisfied. Since the mass of the microsphere scales with the cube of the radius *R*, beads with radii larger than 5 μm possess a mass comparable to the mass of the cantilever, and in some cases, especially with stiffer, shorter cantilevers, even larger. These conditions lead to the failure of the assumption that the mass of the cantilever is uniformly distributed along its length, resulting in an underestimation of the spring constant.

According to Ref.[106], it is possible to correct the apparent spring constant K_0^{th} measured by the thermal noise method using the formula:

$$K^{th} = \frac{\beta}{\beta_0} K_0^{th}$$

where K^{th} is the corrected spring constant, while for rectangular cantilevers $\beta_0 = 0.817$. β depends on the reduced mass of the sphere $\tilde{m}$, i.e. the ratio of the mass of the sphere m_S to the mass of the cantilever m_C, and on the reduced gyration radius of the sphere $\tilde{r}$, proportional to the ratio of the radius *R* of the sphere to the length *L* of the cantilever. For small tips, $\tilde{m}$ and $\tilde{r}$ are negligibly small, and $\beta = \beta_0$, therefore $K^{th} \cong K_0^{th}$. In our case, since L = 350 μm, $m_C = 2.65\times10^3$ ng, $m_S = 1.05\times10^3$ ng, we had $\tilde{m}$ = 0.4 and $\tilde{r}$ = 0.03, therefore corrections were needed.

3.2 Production of nanotopographical and reference CPs

Deposition of the ns-ZrO_2 film on the CP. For the production of nt-CPs, ns-ZrO_2 films are deposited on the colloidal probes exploiting an SCBD apparatus equipped with a Pulsed Microplasma Cluster Source (PMCS)[107,108] (see Supplementary Information, Figure S1). Partially oxidised zirconia clusters are produced within the PMCS and then extracted into the vacuum through a nozzle to form

a seeded supersonic beam. Clusters are collected directly on the CPs intercepting the beam, in the deposition chamber. Upon landing on the probe surface, which is locally flat due to the large radius, clusters form a nanostructured, highly porous, high-specific area, biocompatible ns-ZrO_2 film[47,61,62,82,109]. The oxidation of the nanostructured film further proceeds upon exposure to air, up to an almost complete stoichiometry, although rich of local defects. The crystalline phase is cubic at room temperature[65].

The root mean square (rms) roughness r_q of the deposited film, defined as the standard deviation of surface height values, evolves with the film thickness *h*, according to the power law[62,63] $r_q \sim h^b$, where $b = 0.35$ approximately (details about the evolution of the roughness-thickness relation and on the mechanical stability of the nanostructured thin film can be found in the Supplementary Information, Figures S2, S3)[63,65]. Therefore, by controlling the thickness of the film deposited using a quartz microbalance placed inside the deposition chamber, it is possible to produce nanotopographical CPs with very high reproducibility. The typical thickness of the ns-ZrO_2 films deposited on CPs was in the 70 - 250 nm range, corresponding to roughness values in the range 13-20 nm.

Deposition of smooth ZrO_2 films on the CP. Thin, compact and very smooth coatings of ZrO_2 (flat-$Zr0_2$) with rms roughness below 1 nm were deposited by ion sputtering on the CPs, in order to produce reference interacting surfaces, without any nanotopographical cues. To this purpose, a Kaufman ion gun (Cyberis 40-f) was used to sputter a Zr target. The produced coating is partially oxidised in the deposition chamber; oxidation further proceeds upon exposure to ambient air.

Production of Poly-L-lysine –coated CPs. Also for reference purposes, CPs were coated with poly-L-lysine (PLL). PLL is a poly-amino acid routinely used to facilitate protein adsorption and the attachment of cells to solid surfaces in biological applications, including our previous experiments with PC12 cells[47,67]. For the PLL coating, the probes were incubated with a 0.1% (w/v) PLL solution (Sigma-Aldrich) at room temperature for 30 min, and washed thoroughly afterwards with milliQ water several times before the measurements.

3.3 Force spectroscopy experiments and data analysis

Force spectroscopy. The force spectroscopy experiments were performed using a Bioscope Catalyst AFM (Bruker). During the AFM measurements, the temperature of the medium was maintained at 37°C using a perfusion stage incubator and a temperature controller (Lakeshore 3301,

Ohio, USA). The colloidal probes were incubated with the cell culture medium for >30 min at 37°C before the actual measurements.

The deflection sensitivity was calibrated *in situ* and non-invasively before every experiment by using the previously characterised spring constant as a reference, according to the SNAP procedure described in Ref.[44] The standard approach, i.e. pressing the probe on a stiff surface and measuring the inverse of the slope of the force curve in the contact region, could likely cause contamination of the nt-CP surface and damage of the nanotopographical asperities. Moreover, friction-dependent issues can influence the accuracy of the determination of the deflection sensitivity by the standard contact method, when using large CPs [110].

Sets of raw deflection versus approaching distance curves were acquired at locations on the cells body selected by means of the optical microscope. The raw curves where converted into force versus distance curves (shortly force curves, FCs), rescaling the deflection axis by multiplication by the deflection sensitivity and the cantilever spring constant, and summing the cantilever deflection to the Z-piezo displacement axis[111] (see Figures 1b,c and S4). FCs containing 8192 points each were recorded on cells, with ramp length l = 8 μm, maximum load F_{max} = 1 nN and retraction speed at v_r = 16 μm/s. The pulling speed was kept relatively low to reduce hydrodynamics effects[112].

To measure the early steps of cellular adhesion, we selected five contact times (*cts*): 0, 20, 60, 120, 240 s, accordingly. During the contact time, the Z-piezo position was kept constant using the Z closed-loop feedback mode. Long contact times require a very stable system; this condition is obtained by means of both an active anti-vibration base (DVIA-T45, Daeil Systems) and an acoustic enclosure for the AFM (Schaefer Italy), by controlling the environmental temperature in the laboratory, and by allowing for a long equilibration time (30 min, which served also to allow protein adsorption from the medium, such as fibronectin and vitronectin which are present in the serum supplement, to the probe) before starting the experiments. Figure S5 shows that the drift along the vertical direction during contact of the CP with the sample is very small (max. 20 nm in 240 s), and determines a negligible variation of the applied force.

To reduce the stress on the cells and not to alter their adhesive behaviour, a maximum applied load of 1 nN, corresponding to a pressure of the order of 10 Pa, was set during the acquisition of the FCs. For the same reason, the number of FCs collected per cell was limited (not only because of the very long acquisition time of each curve).

Data analysis. Data processing of the sets of curves was carried out in Matlab (Mathworks) environment using custom routines.

The values of several parameters were calculated for the analysis of the cell-probe detachment mechanisms (Figure S4). In particular, we inferred the maximum cell-probe adhesion force F_a,

defined as the maximum force needed to start the detachment of the probe from the cell, with respect to the zero level of the baseline. The work of detachment W required to separate the nt-CP from the cell, W describes the energy dissipated during the detachment and is calculated integrating the area between zero level and the profile of the force versus distance curve. The maximum detachment force F_a depends on different properties of the cell, such as overall rigidity, cortex tension, cell shape, single binding strength and spacing. Compared to F_a, W provides a more complete, integrated information about the cell adhesion, related to the numbers, lengths and strengths of all bonds formed between the nt-CP and the cell. Moreover, we extracted the mean number of $N_{j,t}$ and strength $F_{j,t}$ of the single unbinding events, defined as the difference in force measured before and after the detaching event, of every FC measured[52] (for both, jumps j, and tethers t). The unbinding events must be identified in the retraction section of the FCs[113,114]: we exploited the numerical derivative of the curves with respect to the tip-sample distance[115] (see Supplementary Information, Figure S4) to detect the location of the events.

Statistics and error analysis. Mean values ψ_{mean} and associated errors σ_{mean} (based on the standard deviation of the mean) were calculated for each observable $\psi(F_a, W, N_{j,t}, \ldots)$, as described in detail in the Supplementary Information. These values and errors represent a population of cells in a given condition. To this purpose, first mean values and errors have been calculated for the single cells tested, then these values have been averaged and the resulting error calculated.

Every condition/probe has been tested twice, in two separated days. For every condition/probe at every experimentation day, 5 cells per contact time have been measured by collecting 3 FCs on each cell. The reason behind this procedure is that the measurements for obtaining complete data sets for the long interaction time (i.e. contact time) are quite time-consuming. Therefore, we decided to collect this number of force curves per condition to be able to secure at each day a consistent and complete volume of data, and to repeat the measurements during a second day in the same conditions for statistical purposes. Every condition/probe has thus been tested twice, in two separated days, with physically different, yet equivalent, in term of surface properties, probes. This results in 10 cells per probe/condition per contact time, i.e. 30 single force curves per probe condition per contact time. Once we have tested the equivalence of sets of data acquired in the same conditions in different days, we have averaged over the collection of equivalent FCs (i.e. the 30 FCs acquired with the same probe/condition, same contact time). In the case of inhibition the β1 integrin activity 7-10 cells per condition per contact time have been tested.

We performed two tailed t-tests for assessing the significance of differences of mean values, as indicated in the main text, where we report the p values. For sake of clarity of the figures, significance levels were only mentioned in the captions, but not indicated in the figures.

3.4 Cell Culture and preparation for the force spectroscopy experiments

As cellular model we used neuron-like PC12 cells (i.e., in particular the PC12-Adh clone, ATCC Catalogue No. CRL-1721.1TM). The choice of this cellular model was founded in the fact that we knew from previous studies that these cells interact with ns-ZrO_2 films and react with mechanotransductive responses to the provided nanotopographical stimuli (i.e. r_q = 15 nm)[47,61,67].

For routine cell culture (subculturing every 2-3 days), the cells were kept in an incubator (Galaxy S, RS Biotech) at 37°C and 5% CO_2, in RPMI-1640 medium supplemented with 10% horse serum, 5% fetal bovine serum, 2 mM L-Glutamine, 10 mM HEPES, 100 units/mL penicillin, 1 mM pyruvic acid, and 100 µg/mL streptomycin (all reagents from Sigma Aldrich, if not stated otherwise).

For the force spectroscopy experiments, the cells were detached from the cell culture flasks with trypsin/EDTA solution, counted with an improved Neubauer chamber, and plated in low concentration of 4.000 cells/cm^2 (to guarantee the presence of single separated cells) on Ø 40 mm glass-bottom dishes for cell culture (Willco Wells) the day before the experiment. Phenol-red free solutions were used for the experiments, since this molecule was found to be harmful for the AFM tip holder. Directly before the cell plating, the Ø 40 mm glass-bottom dishes were coated with PLL (incubation with a 0.1% PLL solution for 30 min at RT, followed by several washing steps with PBS) and sterilised with UV light for 10 min. After cell plating, the cells were kept overnight in the incubator to guarantee good cell attachment before the force spectroscopy experiments.

For the integrin activation, the cells were pre-incubated with manganese chloride ($MnCl_2$) at a concentration of 1 mM for >10 min before the measurements (the treatment has been labelled Mn^{2+} in figures). In case of inhibition of the β1 integrin activity, the cells were pre-incubated with the inhibitory 4b4 antibody (Beckman Coulter) at a concentration of 5 µg/mL for >15 min before the measurements (the treatment has been labelled 4b4 in the figures).

4. CONCLUSIONS

Integrin-mediated mechanosensing and mechanotransduction is regulated by biophysical properties of the cellular microenvironment, such as e.g. the nanotopography of the ECM, as it influences the spatial and geometrical organisation of potential cellular adhesion sites[7–10,30]. However, a precise understanding of the spatiotemporal dynamics and molecular actions in the cell/microenvironment interface during adhesion is still elusive, because these events take place at the nanometre scale and involve pN range forces, whose exploration requires sophisticated methodologies. Moreover, an accurate control over the nanotopographical features of the microenvironment is essential, in order to systematically investigate and precisely assess the influence of the different nanotopographical motifs on the mechanotransductive process.

In this framework, we were able to study and quantify the impact of microenvironmental nanotopography on early cellular adhesion events by means of adhesion force spectroscopy based on novel colloidal probes mimicking the nanotopography of natural ECMs. Our approach merges the sensitivity of AFM-based force spectroscopy[38,51] with the possibility of controlling the nanotopographical features of the ECM-mimicking substrate provided by Supersonic Cluster Beam Deposition[61].

Thanks to our innovative approach, we could detect nanotopography-specific modulations of the molecular force loading dynamics and integrin clustering at the level of single binding events, in the critical time window of nascent adhesion formation. Following this approach, we found that the availability of activated integrins is a critical regulatory factor for these nanotopography-dependent dynamics.

Our results are in agreement with the reported importance of force loading[19] for cellular spatial sensing of the microenvironment, and integrin nanocluster bridging between adjacent (tens of nm) adhesion arrays[89].

For the current work, we compared flat (flat-ZrO_2) and nanostructured zirconia (ns-ZrO_2) with the specific roughness parameter r_q = 15 nm, i.e. the two conditions which have shown the most divergent cellular responses in PC12 cells in terms of their impact on differentiative and mechanotransductive processes, according to our previous work[47,61,67]. After this proof-of-principle, which demonstrated that we can detect meaningful differences with this approach, we plan to compare nanotopographies with more subtle variations in the roughness parameter in the future. For this purpose we can exploit the fine control of the surface topography of the nanostructured colloidal probes to dissect in more detail the precise role of morphological properties (such as, e.g., roughness, asperities diameter/distance, or correlation length) in spatiotemporal cell adhesion dynamics, in particular focusing the attention on the clustering of integrin adhesion complexes[47] and force loading in the molecular clutches. Nanotopographical colloidal probes could also be used to examine how

aberrations in components of the mechanotransductive machinery alter the force loading dynamics of cellular adhesion.

Additional features of nt-CPs make them suitable for the investigation of nanoscale phenomena of nanobiotechnological interest. Due to their large area, nt-CPs allows to optically probe the interaction interface, which is particular useful when using fluorescence microscopy and suitable staining of the actin cytoskeleton to image the focal adhesion spots. Moreover, nt-CPs could be used as nanotopographical templates for carrying out further functionalisations, for example by grafting to the corrugated surface biochemical moieties relevant to mechanotransduction, such as ligands, ECM motifs, etc. Apart from the cell biology framework, we think these probes have a good potential if used in physics of matter experiments, e.g. in the context of nanofriction[116], DLVO theory[82,117] or adhesive contact mechanics at disordered, nanostructured interfaces[118,119].

Acknowledgements

We acknowledge the support of the European Union's Horizon 2020 research and innovation programme under the Marie Skłodowska-Curie grant agreement No 812772, project Phys2BioMed, and under the FET Open grant agreement No. 801126, project EDIT. PM and CS acknowledge support from the European Union FP7-NMP-2013-LARGE-7 "FutureNanoNeeds" programme.

We thank Francesca Borghi for support in the characterisation of CPs, Paolo Piseri for useful suggestions for the deposition of thin films by ion beam sputtering, and Mirko D'Urso for support in cell culture. We thank Dr. Stefano Marchesi and Dr. Stefania Marcotti for critical reading of the manuscript.

Author contributions

Conceptualisation: CS, AP; methodology - probe fabrication and characterisation: MC, AP, CP; methodology - cell culture and preparation: TD, CS; methodology - AFM spectroscopy: MC, TD, AP; data curation and analysis: MC, CS, AP; original draft writing: MC, CS, AP; draft reviewing and editing: MC, CS, AP, CL, PM; supervision: CL, PM, CS, AP; resources, funding and project administration: CL, PM, AP. Author contributions were allocated adopting the terminology of CRediT - Contributor Roles Taxonomy.

5. BIBLIOGRAPHY

1 T. Maurer, M. H. Stoffel, Y. Belyaev, N. G. Stiefel, B. Vidondo, S. Küker, H. Mogel, B. Schäfer and J. Balmer, *PLOS ONE*, 2018, **13**, e0205027.

2 J. Park, D.-H. Kim and A. Levchenko, *Biophys. J.*, 2018, **114**, 1257–1263.

3 Z. Lansky, Y. Mutsafi, L. Houben, T. Ilani, G. Armony, S. G. Wolf and D. Fass, *J. Struct. Biol. X*, 2019, **1**, 100002.

4 S. J. Liliensiek, P. Nealey and C. J. Murphy, *Tissue Eng. Part A*, 2009, **15**, 2643–2651.

5 M. Tajerian, V. Hung, H. Nguyen, G. Lee, L.-M. Joubert, A. V. Malkovskiy, B. Zou, S. Xie, T.-T. Huang and J. D. Clark, *Mol. Psychiatry*, 2018, **23**, 2302–2313.

6 G. A. Abrams, S. L. Goodman, P. F. Nealey, M. Franco and C. J. Murphy, *Cell Tissue Res.*, 2000, **299**, 39–46.

7 M. J. Dalby, N. Gadegaard and R. O. C. Oreffo, *Nat. Mater.*, 2014, **13**, 558–569.

8 J. Z. Gasiorowski, C. J. Murphy and P. F. Nealey, *Annu. Rev. Biomed. Eng.*, 2013, **15**, 155–176.

9 J. L. Young, A. W. Holle and J. P. Spatz, *Exp. Cell Res.*, 2016, **343**, 3–6.

10 S. W. Crowder, V. Leonardo, T. Whittaker, P. Papathanasiou and M. M. Stevens, *Cell Stem Cell*, 2016, **18**, 39–52.

11 C. C. DuFort, M. J. Paszek and V. M. Weaver, *Nat. Rev. Mol. Cell Biol.*, 2011, **12**, 308–319.

12 Z. Sun, S. S. Guo and R. Fässler, *J Cell Biol*, 2016, jcb.201609037.

13 R. Changede and M. Sheetz, *BioEssays*, 2017, **39**, n/a-n/a.

14 N. C. Gauthier and P. Roca-Cusachs, *Curr. Opin. Cell Biol.*, 2018, **50**, 20–26.

15 T. Orré, O. Rossier and G. Giannone, *Exp. Cell Res.*, 2019, **379**, 235–244.

16 J. Z. Kechagia, J. Ivaska and P. Roca-Cusachs, *Nat. Rev. Mol. Cell Biol.*, 2019, 1.

17 M. Chighizola, T. Dini, C. Lenardi, P. Milani, A. Podestà and C. Schulte, *Biophys. Rev.*, , DOI:10.1007/s12551-019-00587-2.

18 J. D. Humphries, M. R. Chastney, J. A. Askari and M. J. Humphries, *Curr. Opin. Cell Biol.*, 2019, **56**, 14–21.

19 R. Oria, T. Wiegand, J. Escribano, A. Elosegui-Artola, J. J. Uriarte, C. Moreno-Pulido, I. Platzman, P. Delcanale, L. Albertazzi, D. Navajas, X. Trepat, J. M. García-Aznar, E. A. Cavalcanti-Adam and P. Roca-Cusachs, *Nature*, 2017, **552**, 219.

20 D. E. Ingber, *Ann. Med.*, 2003, **35**, 564–577.

21 M. J. Paszek, N. Zahir, K. R. Johnson, J. N. Lakins, G. I. Rozenberg, A. Gefen, C. A. Reinhart-King, S. S. Margulies, M. Dembo, D. Boettiger, D. A. Hammer and V. M. Weaver, *Cancer Cell*, 2005, **8**, 241–254.

22 D. E. Jaalouk and J. Lammerding, *Nat. Rev. Mol. Cell Biol.*, 2009, **10**, 63–73.

23 M. Nebuloni, L. Albarello, A. Andolfo, C. Magagnotti, L. Genovese, I. Locatelli, G. Tonon, E. Longhi, P. Zerbi, R. Allevi, A. Podestà, L. Puricelli, P. Milani, A. Soldarini, A. Salonia and M. Alfano, *Sci. Rep.*, 2016, **6**, 22522.

24 V. Vogel, *Annu. Rev. Physiol.*, 2018, **80**, 353–387.

25 J. Guck, *Biophys. Rev.*, 2019, **11**, 667–670.

26 A. W. Holle, J. L. Young, K. J. Van Vliet, R. D. Kamm, D. Discher, P. Janmey, J. P. Spatz and T. Saif, *Nano Lett.*, 2018, **18**, 1–8.

27 B. K. K. Teo, S. T. Wong, C. K. Lim, T. Y. S. Kung, C. H. Yap, Y. Ramagopal, L. H. Romer and E. K. F. Yim, *ACS Nano*, 2013, **7**, 4785–4798.

28 D. Carson, M. Hnilova, X. Yang, C. L. Nemeth, J. H. Tsui, A. S. T. Smith, A. Jiao, M. Regnier, C. E. Murry, C. Tamerler and D.-H. Kim, *ACS Appl. Mater. Interfaces*, 2016, **8**, 21923–21932.

29 K. Yang, K. Jung, E. Ko, J. Kim, K. I. Park, J. Kim and S.-W. Cho, *ACS Appl. Mater. Interfaces*, 2013, **5**, 10529–10540.

30 W. Chen, Y. Shao, X. Li, G. Zhao and J. Fu, *Nano Today*, 2014, **9**, 759–784.

31 F. Variola, J. B. Brunski, G. Orsini, P. T. de Oliveira, R. Wazen and A. Nanci, *Nanoscale*, 2011, **3**, 335–353.
32 J. Huang, S. V. Grater, F. Corbellini, S. Rinck, E. Bock, R. Kemkemer, H. Kessler, J. Ding and J. P. Spatz, *Nano Lett.*, 2009, **9**, 1111–1116.
33 E. Ngandu Mpoyi, M. Cantini, P. M. Reynolds, N. Gadegaard, M. J. Dalby and M. Salmerón-Sánchez, *ACS Nano*, 2016, **10**, 6638–6647.
34 P. M. Mendes, *Chem. Soc. Rev.*, 2013, **42**, 9207–9218.
35 T. Iskratsch, H. Wolfenson and M. P. Sheetz, *Nat. Rev. Mol. Cell Biol.*, 2014, **15**, 825–833.
36 L. Li, J. Eyckmans and C. S. Chen, *Nat. Mater.*, 2017, **16**, 1164–1168.
37 M. Darnell and D. J. Mooney, *Nat. Mater.*, 2017, **16**, 1178–1185.
38 M. Krieg, G. Fläschner, D. Alsteens, B. M. Gaub, W. H. Roos, G. J. L. Wuite, H. E. Gaub, C. Gerber, Y. F. Dufrêne and D. J. Müller, *Nat. Rev. Phys.*, 2019, **1**, 41.
39 K. Amschler, L. Erpenbeck, S. Kruss and M. P. Schön, *ACS Nano*, 2014, **8**, 9113–9125.
40 A. C. Chang, A. H. Mekhdjian, M. Morimatsu, A. K. Denisin, B. L. Pruitt and A. R. Dunn, *ACS Nano*, 2016, **10**, 10745–10752.
41 J. N. Roberts, J. K. Sahoo, L. E. McNamara, K. V. Burgess, J. Yang, E. V. Alakpa, H. J. Anderson, J. Hay, L.-A. Turner, S. J. Yarwood, M. Zelzer, R. O. C. Oreffo, R. V. Ulijn and M. J. Dalby, *ACS Nano*, 2016, **10**, 6667–6679.
42 Y. F. Dufrêne and A. E. Pelling, *Nanoscale*, 2013, **5**, 4094–4104.
43 M. Radmacher, in *Methods in Cell Biology*, Academic Press, 2007, vol. 83, pp. 347–372.
44 H. Schillers, C. Rianna, J. Schäpe, T. Luque, H. Doschke, M. Wälte, J. J. Uriarte, N. Campillo, G. P. A. Michanetzis, J. Bobrowska, A. Dumitru, E. T. Herruzo, S. Bovio, P. Parot, M. Galluzzi, A. Podestà, L. Puricelli, S. Scheuring, Y. Missirlis, R. Garcia, M. Odorico, J.-M. Teulon, F. Lafont, M. Lekka, F. Rico, A. Rigato, J.-L. Pellequer, H. Oberleithner, D. Navajas and M. Radmacher, *Sci. Rep.*, , DOI:10.1038/s41598-017-05383-0.
45 L. Puricelli, M. Galluzzi, C. Schulte, A. Podestà and P. Milani, *Rev. Sci. Instrum.*, 2015, **86**, 033705.
46 A. Stylianou, M. Lekka and T. Stylianopoulos, *Nanoscale*, 2018, **10**, 20930–20945.
47 C. Schulte, S. Rodighiero, M. A. Cappelluti, L. Puricelli, E. Maffioli, F. Borghi, A. Negri, E. Sogne, M. Galluzzi, C. Piazzoni, M. Tamplenizza, A. Podestà, G. Tedeschi, C. Lenardi and P. Milani, *J. Nanobiotechnology*, 2016, **14**, 18.
48 G. M. S. Ferraris, C. Schulte, V. Buttiglione, V. De Lorenzi, A. Piontini, M. Galluzzi, A. Podestà, C. D. Madsen and N. Sidenius, *EMBO J.*, 2014, **33**, 2458–2472.
49 C. Schulte, G. M. S. Ferraris, A. Oldani, M. Galluzzi, A. Podestà, L. Puricelli, V. de Lorenzi, C. Lenardi, P. Milani and N. Sidenius, *Eur. J. Cell Biol.*, 2016, **95**, 1–14.
50 Y. F. Dufrêne, E. Evans, A. Engel, J. Helenius, H. E. Gaub and D. J. Müller, *Nat. Methods*, 2011, **8**, 123–127.
51 D. J. Müller, J. Helenius, D. Alsteens and Y. F. Dufrêne, *Nat. Chem. Biol.*, 2009, **5**, 383–390.
52 J. Friedrichs, K. R. Legate, R. Schubert, M. Bharadwaj, C. Werner, D. J. Müller and M. Benoit, *Methods*, 2013, **60**, 169–178.
53 N. Strohmeyer, M. Bharadwaj, M. Costell, R. Fässler and D. J. Müller, *Nat. Mater.*, 2017, **16**, 1262–1270.
54 F. Li, S. D. Redick, H. P. Erickson and V. T. Moy, *Biophys. J.*, 2003, **84**, 1252–1262.
55 A. Taubenberger, D. A. Cisneros, J. Friedrichs, P.-H. Puech, D. J. Muller and C. M. Franz, *Mol. Biol. Cell*, 2007, **18**, 1634–1644.
56 M. Tulla, J. Helenius, J. Jokinen, A. Taubenberger, D. J. Müller and J. Heino, *FEBS Lett.*, 2008, **582**, 3520–3524.
57 P. Bertoncini, S. L. Chevalier, S. Lavenus, P. Layrolle and G. Louarn, *J. Mol. Recognit.*, 2012, **25**, 262–269.

58 C. Selhuber-Unkel, M. López-García, H. Kessler and J. P. Spatz, *Biophys. J.*, 2008, **95**, 5424–5431.
59 C. Selhuber-Unkel, T. Erdmann, M. López-García, H. Kessler, U. S. Schwarz and J. P. Spatz, *Biophys. J.*, 2010, **98**, 543–551.
60 T. Naganuma, *Nanoscale*, 2017, **9**, 13171–13186.
61 C. Schulte, A. Podestà, C. Lenardi, G. Tedeschi and P. Milani, *Acc. Chem. Res.*, 2017, **50**, 231–239.
62 F. Borghi, E. Sogne, C. Lenardi, A. Podestà, M. Merlini, C. Ducati and P. Milani, *J. Appl. Phys.*, 2016, **120**, 055302.
63 F. Borghi, A. Podestà, C. Piazzoni and P. Milani, *Phys. Rev. Appl.*, 2018, **9**, 044016.
64 P. F. Manicone, P. Rossi Iommetti and L. Raffaelli, *J. Dent.*, 2007, **35**, 819–826.
65 F. Borghi, E. Sogne, C. Lenardi, A. Podestà, M. Merlini, C. Ducati and P. Milani, *J. Appl. Phys.*, 2016, **120**, 055302.
66 C. Schulte, M. Ripamonti, E. Maffioli, M. A. Cappelluti, S. Nonnis, L. Puricelli, J. Lamanna, C. Piazzoni, A. Podestà, C. Lenardi, G. Tedeschi, A. Malgaroli and P. Milani, *Front. Cell. Neurosci.*, 2016, **10**, 267.
67 E. Maffioli, C. Schulte, S. Nonnis, F. Grassi Scalvini, C. Piazzoni, C. Lenardi, A. Negri, P. Milani and G. Tedeschi, *Front. Cell. Neurosci.*, , DOI:10.3389/fncel.2017.00417.
68 M. Arnold, E. A. Cavalcanti-Adam, R. Glass, J. Blümmel, W. Eck, M. Kantlehner, H. Kessler and J. P. Spatz, *Chemphyschem Eur. J. Chem. Phys. Phys. Chem.*, 2004, **5**, 383–388.
69 E. A. Cavalcanti-Adam, A. Micoulet, J. Blümmel, J. Auernheimer, H. Kessler and J. P. Spatz, *Eur. J. Cell Biol.*, 2006, **85**, 219–224.
70 E. A. Cavalcanti-Adam, T. Volberg, A. Micoulet, H. Kessler, B. Geiger and J. P. Spatz, *Biophys. J.*, 2007, **92**, 2964–2974.
71 C. Schulte, J. Lamanna, A. S. Moro, C. Piazzoni, F. Borghi, M. Chighizola, S. Ortoleva, G. Racchetti, C. Lenardi, A. Podestà, A. Malgaroli and P. Milani, *ACS Biomater. Sci. Eng.*, 2018, **4**, 4062–4075.
72 R. W. N. Nugroho, R. Harjumäki, X. Zhang, Y.-R. Lou, M. Yliperttula, J. J. Valle-Delgado and M. Österberg, *Colloids Surf. B Biointerfaces*, 2019, **173**, 571–580.
73 L. Chièze, A. L. Cigne, M. Meunier, A. Berquand, S. Dedieu, J. Devy and M. Molinari, *J. Mol. Recognit.*, 2019, **32**, e2767.
74 J. K. Vasir and V. Labhasetwar, *Biomaterials*, 2008, **29**, 4244–4252.
75 Q. K. Ong and I. Sokolov, *J. Colloid Interface Sci.*, 2007, **310**, 385–390.
76 G. Pyrgiotakis, C. O. Blattmann and P. Demokritou, *ACS Sustain. Chem. Eng.*, 2014, **2**, 1681–1690.
77 Z. Leonenko, E. Finot and M. Amrein, *Ultramicroscopy*, 2007, **107**, 948–953.
78 A. Podestà, F. Borghi, M. Indrieri, S. Bovio, C. Piazzoni and P. Milani, *J. Appl. Phys.*, 2015, **118**, 234309.
79 L. Gailite, P. E. Scopelliti, V. K. Sharma, M. Indrieri, A. Podestà, G. Tedeschi and P. Milani, *Langmuir*, 2014, **30**, 5973–5981.
80 P. E. Scopelliti, A. Borgonovo, M. Indrieri, L. Giorgetti, G. Bongiorno, R. Carbone, A. Podestà and P. Milani, *PLOS ONE*, 2010, **5**, e11862.
81 A. Bachhuka, J. D. Hayball, L. E. Smith and K. Vasilev, *ACS Appl. Mater. Interfaces*, 2017, **9**, 5874–5884.
82 F. Borghi, B. Scaparra, C. Paternoster, P. Milani and A. Podestà, *Langmuir*, 2018, **34**, 10230–10242.
83 E. A. Evans and D. A. Calderwood, *Science*, 2007, **316**, 1148–1153.
84 E. Sariisik, C. Popov, J. P. Müller, D. Docheva, H. Clausen-Schaumann and M. Benoit, *Biophys. J.*, 2015, **109**, 1330–1333.
85 A. Mescola, S. Vella, M. Scotto, P. Gavazzo, C. Canale, A. Diaspro, A. Pagano and M.

Vassalli, *J. Mol. Recognit. JMR*, 2012, **25**, 270–277.
86 D. Boettiger and B. Wehrle-Haller, *J. Phys. Condens. Matter Inst. Phys. J.*, 2010, **22**, 194101.
87 M. Vicente-Manzanares and A. R. Horwitz, *J. Cell Sci.*, 2011, **124**, 3923–3927.
88 R. Changede, X. Xu, F. Margadant and M. P. Sheetz, *Dev. Cell*, 2015, **35**, 614–621.
89 R. Changede, H. Cai, S. J. Wind and M. P. Sheetz, *Nat. Mater.*, 2019, 1–10.
90 P. Roca-Cusachs, N. C. Gauthier, A. del Rio and M. P. Sheetz, *Proc. Natl. Acad. Sci.*, 2009, **106**, 16245–16250.
91 O. Rossier, V. Octeau, J.-B. Sibarita, C. Leduc, B. Tessier, D. Nair, V. Gatterdam, O. Destaing, C. Albigès-Rizo, R. Tampé, L. Cognet, D. Choquet, B. Lounis and G. Giannone, *Nat. Cell Biol.*, 2012, **14**, 1057–1067.
92 H. B. Schiller, M.-R. Hermann, J. Polleux, T. Vignaud, S. Zanivan, C. C. Friedel, Z. Sun, A. Raducanu, K.-E. Gottschalk, M. Théry, M. Mann and R. Fässler, *Nat. Cell Biol.*, 2013, **15**, 625–636.
93 A. Elosegui-Artola, E. Bazellières, M. D. Allen, I. Andreu, R. Oria, R. Sunyer, J. J. Gomm, J. F. Marshall, J. L. Jones, X. Trepat and P. Roca-Cusachs, *Nat. Mater.*, 2014, **13**, 631–637.
94 H. E. Balcioglu, H. van Hoorn, D. M. Donato, T. Schmidt and E. H. J. Danen, *J. Cell Sci.*, 2015, **128**, 1316–1326.
95 M. Bharadwaj, N. Strohmeyer, G. P. Colo, J. Helenius, N. Beerenwinkel, H. B. Schiller, R. Fässler and D. J. Müller, *Nat. Commun.*, 2017, **8**, 14348.
96 Z. Sun, L. A. Martinez-Lemus, A. Trache, J. P. Trzeciakowski, G. E. Davis, U. Pohl and G. A. Meininger, *Am. J. Physiol. Heart Circ. Physiol.*, 2005, **289**, H2526-2535.
97 F. Kong, A. J. García, A. P. Mould, M. J. Humphries and C. Zhu, *J. Cell Biol.*, 2009, **185**, 1275–1284.
98 X. Wang and T. Ha, *Science*, 2013, **340**, 991–994.
99 Y. Liu, K. Yehl, Y. Narui and K. Salaita, *J. Am. Chem. Soc.*, 2013, **135**, 5320–5323.
100 K. Galior, Y. Liu, K. Yehl, S. Vivek and K. Salaita, *Nano Lett.*, 2016, **16**, 341–348.
101 M. Yao, B. T. Goult, H. Chen, P. Cong, M. P. Sheetz and J. Yan, *Sci. Rep.*, 2014, **4**, 4610.
102 M. Schvartzman, M. Palma, J. Sable, J. Abramson, X. Hu, M. P. Sheetz and S. J. Wind, *Nano Lett.*, 2011, **11**, 1306–1312.
103 M. Indrieri, A. Podestà, G. Bongiorno, D. Marchesi and P. Milani, *Rev. Sci. Instrum.*, 2011, **82**, 023708.
104 J.L. Hutter and J. Bechhoefer, *Rev. Sci. Instrum.*, 1993, **64**, 1868–1873.
105 H.-J. Butt and M. Jaschke, *Nanotechnology*, 1995, **6**, 1–7.
106 J. Laurent, A. Steinberger and L. Bellon, *Nanotechnology*, 2013, **24**, 225504.
107 K. Wegner, P. Piseri, H. V. Tafreshi and P. Milani, *J. Phys. Appl. Phys.*, 2006, **39**, R439.
108 E. Barborini, P. Piseri and P. Milani, *J. Phys. Appl. Phys.*, 1999, **32**, L105.
109 A. Galli, E. Maffioli, E. Sogne, S. Moretti, E. S. D. Cairano, A. Negri, S. Nonnis, G. D. Norata, F. Bonacina, F. Borghi, A. Podestà, F. Bertuzzi, P. Milani, C. Lenardi, G. Tedeschi and C. Perego, *Sci. Rep.*, 2018, **8**, 1–17.
110 P. P. Weafer, J. P. McGarry, M. H. van Es, J. I. Kilpatrick, W. Ronan, D. R. Nolan and S. P. Jarvis, *Rev. Sci. Instrum.*, 2012, **83**, 093709.
111 H.-J. Butt, B. Cappella and M. Kappl, *Surf. Sci. Rep.*, 2005, **59**, 1–152.
112 H. Janovjak, J. Struckmeier and D. J. Müller, *Eur. Biophys. J.*, 2005, **34**, 91–96.
113 B. C. Carter, M. Vershinin and S. P. Gross, *Biophys. J.*, 2008, **94**, 306–319.
114 J. Opfer and K.-E. Gottschalk, *PLOS ONE*, 2012, **7**, e45896.
115 M. Odorico, J.-M. Teulon, O. Berthoumieu, S. -w. W. Chen, P. Parot and J.-L. Pellequer, *Ultramicroscopy*, 2007, **107**, 887–894.
116 B. Bhushan and S. Sundararajan, *Acta Mater.*, 1998, **46**, 3793–3804.
117 F. Borghi, V. Vyas, A. Podestà and P. Milani, *PLOS ONE*, 2013, **8**, e68655.

118 W. Deng and H. Kesari, *Sci. Rep.*, 2019, **9**, 1–12.
119 H. Kesari, J. C. Doll, B. L. Pruitt, W. Cai and A. J. Lew, *Philos. Mag. Lett.*, 2010, **90**, 891–902.

Adhesion force spectroscopy with nanostructured colloidal probes reveals nanotopography-dependent early mechanotransductive interactions at the cell membrane level

M. Chighizola, A. Previdi, T. Dini, C. Piazzoni, C. Lenardi, P. Milani, C. Schulte* and A. Podestà*

C.I.Ma.I.Na. and Dipartimento di Fisica "Aldo Pontremoli",
Università degli Studi di Milano, via Celoria 16, 20133 Milan, Italy.

*Corresponding authors: alessandro.podesta@mi.infn.it; carsten.schulte@unimi.it

SUPPLEMENTARY INFORMATION

Contents

Supersonic Cluster Beam Deposition Apparatus (SCBD)

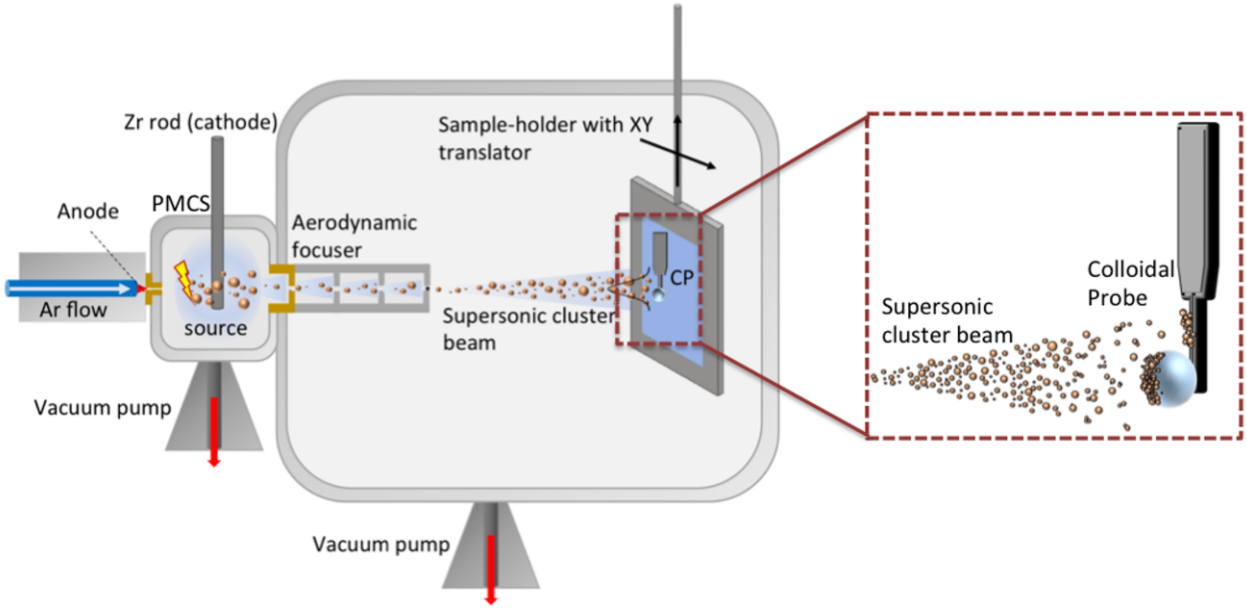

Figure S1. *A schematic representation of the SCBD apparatus that was used for the production of nt-CPs. The Zr rod is sputtered by a plasma discharge, triggered by the introduction of argon (Ar) through a pulsed valve into the source cavity and the application of a high voltage between the Zr rod and the anode. The ablated species condense into clusters and the resulting gas-clusters mixture is extracted through a nozzle and an aerodynamic focuser into a high vacuum chamber; during the process, the carrier gas-clusters mixture undergoes a supersonic expansion. The cluster beam impinges on the CP, where a thin, nanostructured ZrO_2 film is formed.*

Scaling of the surface roughness of ns-ZrO_2 films

To characterise the growth mechanism of ns-ZrO_2 films on colloidal probes (CPs), we dispersed the glass spheres on a flat glass microscopy slide, and deposited ns-ZrO_2 films varying the deposition times. We then imaged the coated CP surfaces by AFM in Tapping Mode (probe model: NCHV, Bruker), with relative scan speed of the tip v_{scan} = 2μm/s, and we measured the rms roughness r_q. The film thickness h was measured on the flat glass surface, in a region close to a sphere, by imaging the ns-ZrO_2 film across a sharp step produced by masking the substrate during deposition. By applying a linear regression on a loglog scale to the r_q versus h curve (see Figure S2), the value of the growth exponent b can be determined as the slope of the curve, according to the equation $r_q \sim h^b$.

According to previous results[1–3], the b parameter of the cluster-assembled ZrO_2 thin films grown on flat substrates is b = 0.368 ± 0.001 on silicon, or b = 0.31 ± 0.09 on glass coated with a monomolecular PAcrAm-*g*-(PMOXA, NH_2, Si) layer[4]. These values are compatible with the prediction of the ballistic deposition growth model (b = 0.32 - 0.25), which assumes that clusters impinge with a direction perpendicular to the plane of the substrate, and they do not diffuse significantly upon landing[5–7]. Higher values can be found when the impinging particles possess a distribution of size and different sticking probabilities.

On nt-CPs, we found b = 0.314 ± 0.017, in agreement with the value measured on flat substrates. Therefore, the curvature of the nt-CPs did not influence the growth exponent.

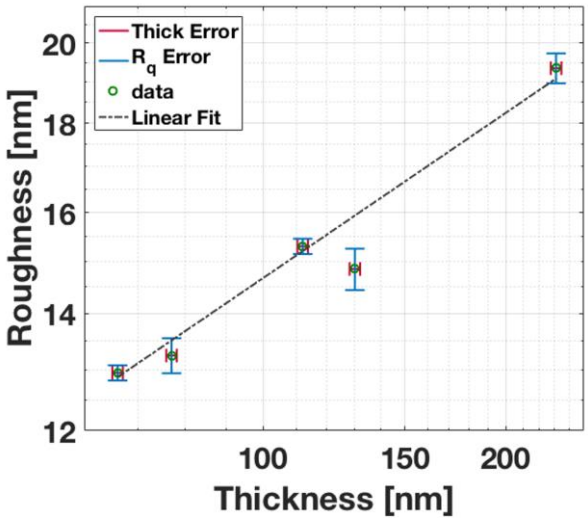

***Figure S2**. Scaling of the rms roughness r_q of ns-ZrO_2 film (i.e. roughness) on the nt-CPs.*

Mechanical stability of ns-ZrO_2 films

To test the mechanical stability of the nanostructured coating we used a stiff AFM tapping mode probe (force constant K = 50. 4 N/m) to apply high forces on the thin film, in order to record at which forces rupture events between ZrO2 nanoparticles take place.

An example of the force curve (FC) with the rupture events detected is shown in Figure S3a, while the rupture forces measured are represented in Figure S3b. Rupture forces are clustered around specific values and it is possible that the higher forces events represent cascade rupture events, where groups of nanoparticles simultaneously detach, while the lower forces represent the tip slipping across a nanoparticle, or small nanoparticles detaching from low-attachment points. The lowest rupture force detected is around F~ 70 nN, that is almost 25 times larger than the highest force measured during the force spectroscopy experiment.

Furthermore, we scanned in Tapping Mode the surface of the contact region of an nt-CP after a whole day of force spectroscopy experiments. The image obtained is shown in Figure S3c, after subtraction of the spherical curvature in order to highlight the morphological details at the nanoscale. The granularity of the surface due to the presence of the ns-ZrO2 thin film is clearly evident.

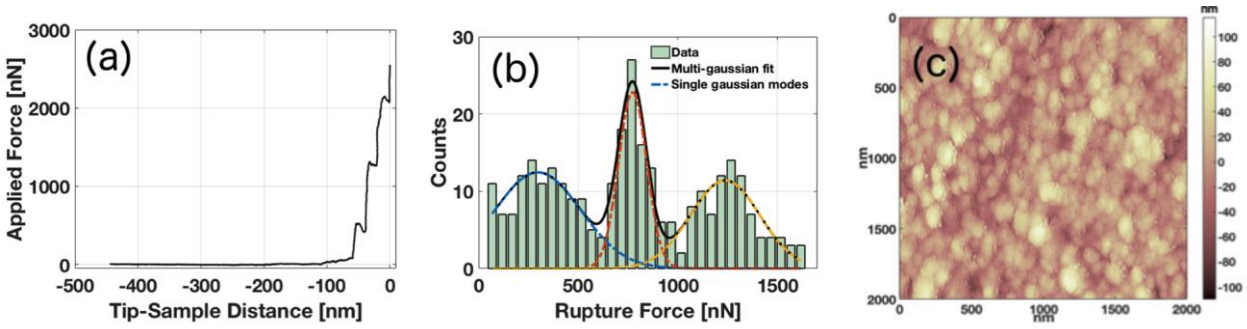

Figure S3*. (a) Representative FC with three rupture events detected; (b) distribution of the rupture event forces from all FCs, with multi-gaussian fit highlighted; (c) scan of the contact surface of a nt-CP after force spectroscopy experiment.*

Data Analysis

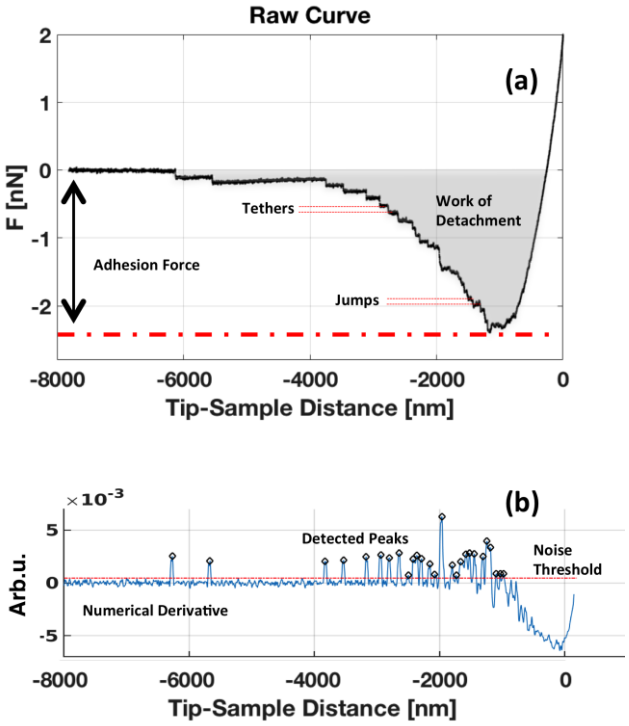

Figure S4. (a) *The retraction part of a representative FC, with the two different possible unbinding events, jumps and tethers, total adhesion force and work of detachment shown.* ***(b)*** *Numerical derivative of the FC used to identify and locate the unbinding events.*

Statistics and error analysis

For each observable ψ_{FCs} extracted by each force curve (FC) a mean value ψ_{cell} was evaluated for each cell. The error σ_{cell} associated to ψ_{cell} was obtained by summing in quadrature the standard deviation of the mean σ_{ψ} of the results coming from the single FCs and an estimated instrumental error $\sigma_{instrum}$ ($\sigma_{instrum} / \psi = 3\%$)[8]:

$$\psi_{cell} = \frac{\sum_i^n \psi_{FCs}}{n}$$

where *n* is the number of force curves per each cell,

$$\sigma_{cell} = \sqrt{\sigma_{\psi}^2 + \sigma_{instrum}^2}$$

The final mean value ψ_{mean} representative of the cell population behaviour in a given condition was evaluated as:

$$\psi_{mean} = \frac{\sum_i^n \psi_{cell}}{N}$$

where *N* is the number of cells investigated for the given condition.

The final error σ_{mean} associated to ψ_{mean} was calculated by summing in quadrature the propagated error of the mean σ_s and the standard deviation of the mean of the singles cell values ψ_{cell}:

$$\sigma_{\mathrm{mean}} = \sqrt{\sigma_{\mathrm{std}}^2 + \sigma_{\mathrm{s}}^2}$$

where

$$\sigma_{\mathrm{s}} = \frac{1}{N}\sqrt{\sum_i \sigma_{cell}^2}\ ,\ \ \sigma_{std} = \sqrt{\frac{\sum_i^n (\psi_{cell,i} - \psi_{fin})^2}{N}}$$

Force curves during contact

To test the stability of the Z-piezo upon contact of the CP with the sample in close-loop mode, we recorded the cantilever deflection as a function of the contact time *t*, up to *t* = 240s.

The time-dependent deflection is shown in Figure S5. On a stiff substrate, a smooth drift is observed (~10 nm in 240 s), corresponding to a maximum variation of the applied force of approximately 0.5 nN after 240s. On the cell surface, a similar drift is observed superimposed to small and slow (tens of nm in tens of seconds) fluctuations, due to the adjustment of the cell below the probe, probably accompanied by internal reorganisation of the cytoskeleton[9].

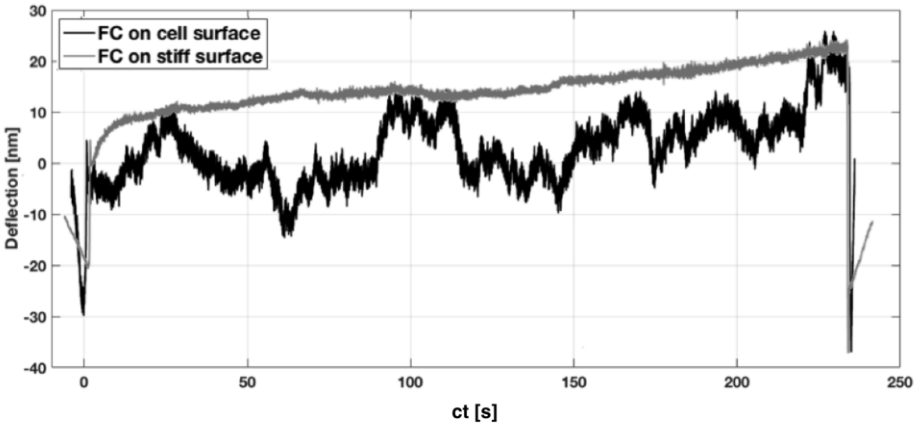

Figure S5. *Representative deflection versus contact time curves.*

Dependence of the adhesion force on the contact times, with the contribution of the tethers

The evaluation of the tether contribution to the total adhesion force F_a was evaluated as follow: for each contact time, the mean value of the tethers unbinding force has been evaluated and multiplied by the mean number of tethers N_t per FC, to obtain the tether background adhesion value.

The contribution of the tethers then has been subtracted from the adhesion force F_a, in order to calculate the contribution of the jumps. The obtained total jump adhesion force was eventually divided by the mean number of jumps N_j, in order to calculate the mean adhesion force per jump presented in Figures 4 and 5 of the main text.

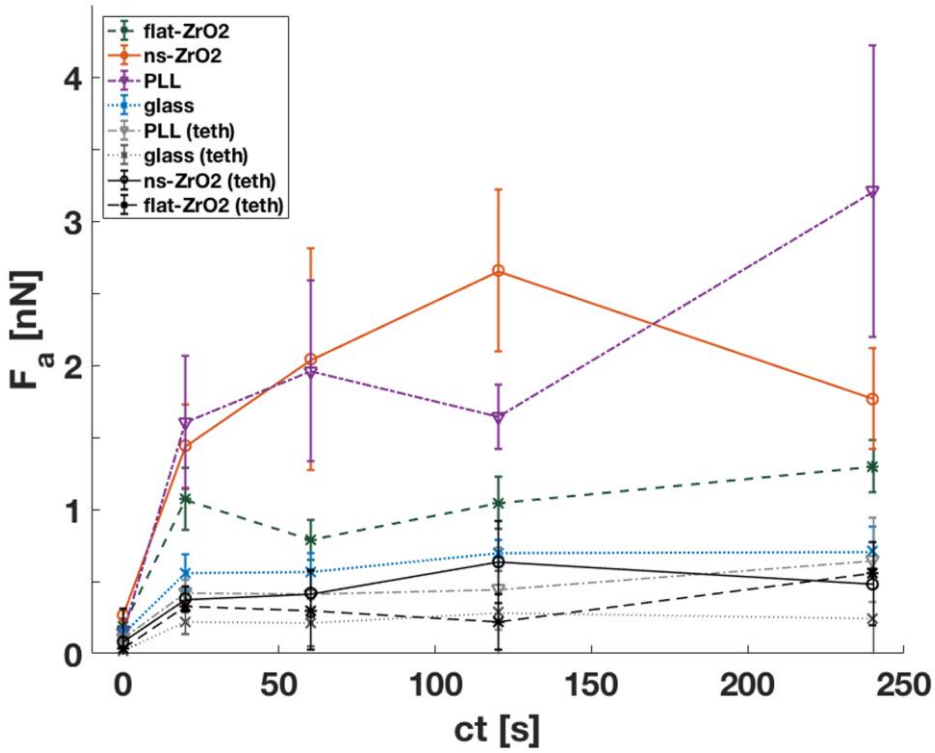

Figure S6. *Dependence of the adhesion force on the contact times as in Figure 3a; in addition, the contribution of the tethers (calculated as described above) is shown.*

Representative retraction force curves at different contact times

We show representative of FCs of the adhesive behaviour of the cells on the different surfaces for contact time *ct* =20s, 60s, 120s.

It is possible to observe the differences in the adhesion force F_a, work of detachment W, and number of jumps N_j, respectively. In particular, it can be seen how the adhesion on the ns-ZrO_2 surface (at ct=60 sec) reaches values compatible to the adhesion on the PLL, even in the presence of much less detachment events.

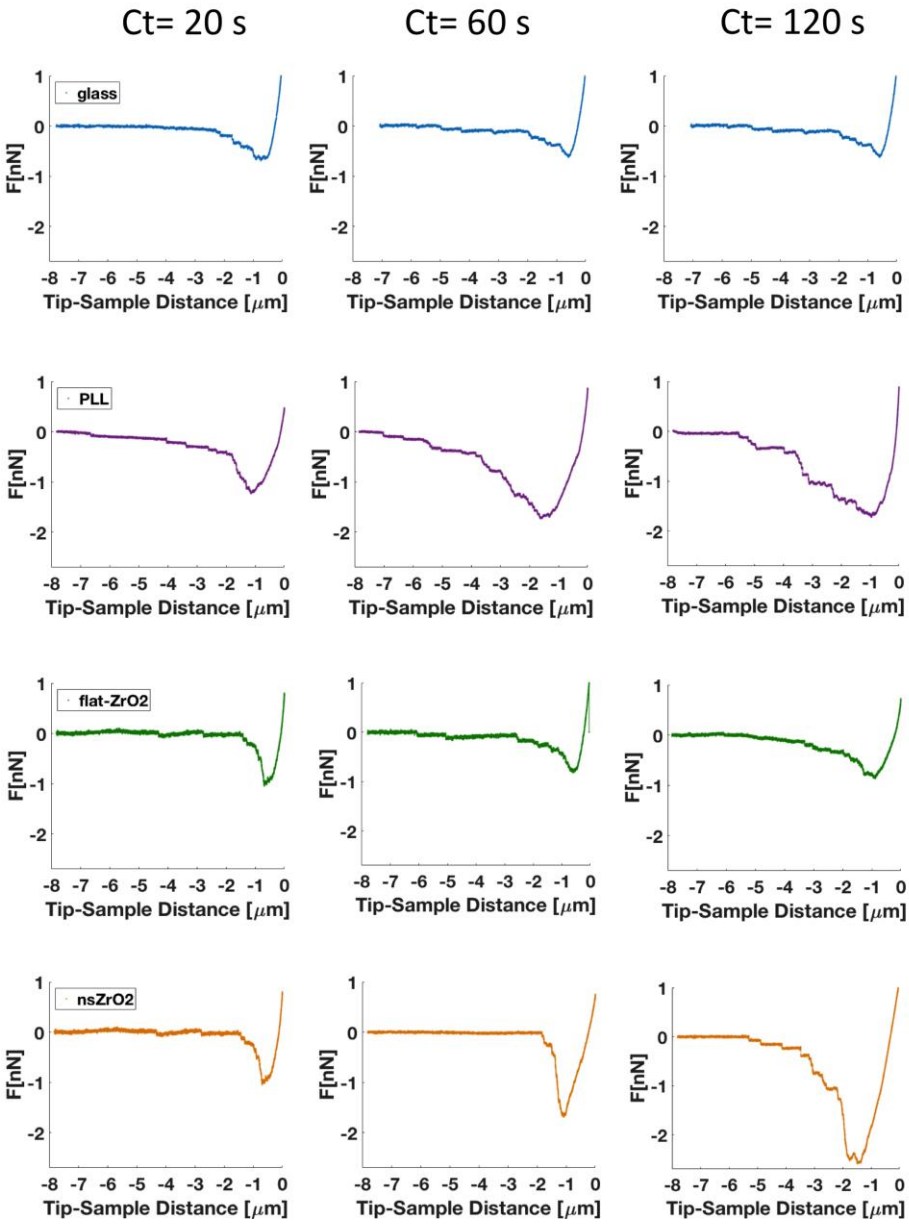

Figure S7*. Representative FCs at ct=20 s, 60 s, 120 s for each condition: glass (blue), PLL (violet), flat-ZrO_2 (green), ns-ZrO_2 (orange).*

Regarding the occurrence of jump events over a longer distance in the PLL condition, it must be pointed out that the positive charge of the PLL coating may favour on the one hand unspecific, electrostatic binding events of surface receptors, and on the other hand the polymeric nature of PLL with its long chains can unfold and be pulled away from the probe surface. This could favour detachment events occurring at higher separations, compared to the other conditions. In the PLL condition, the jump events could therefore more frequently be caused also by non-integrin surface receptors that are in some way attached to the cytoskeleton, as e.g. CD44 or syndecan-4. However, for the moment being we can only speculate about this.

Bibliography

(1) Borghi, F.; Podestà, A.; Piazzoni, C.; Milani, P. Growth Mechanism of Cluster-Assembled Surfaces: From Submonolayer to Thin-Film Regime. *Phys. Rev. Appl.* **2018**, *9* (4), 044016. https://doi.org/10.1103/PhysRevApplied.9.044016.

(2) Borghi, F.; Sogne, E.; Lenardi, C.; Podestà, A.; Merlini, M.; Ducati, C.; Milani, P. Cluster-Assembled Cubic Zirconia Films with Tunable and Stable Nanoscale Morphology against Thermal Annealing. *J. Appl. Phys.* **2016**, *120* (5), 055302. https://doi.org/10.1063/1.4960441.

(3) Podestà, A.; Borghi, F.; Indrieri, M.; Bovio, S.; Piazzoni, C.; Milani, P. Nanomanufacturing of Titania Interfaces with Controlled Structural and Functional Properties by Supersonic Cluster Beam Deposition. *J. Appl. Phys.* **2015**, *118* (23), 234309. https://doi.org/10.1063/1.4937549.

(4) Schulte, C.; Lamanna, J.; Moro, A. S.; Piazzoni, C.; Borghi, F.; Chighizola, M.; Ortoleva, S.; Racchetti, G.; Lenardi, C.; Podestà, A.; et al. Neuronal Cells Confinement by Micropatterned Cluster-Assembled Dots with Mechanotransductive Nanotopography. *ACS Biomater. Sci. Eng.* **2018**, *4* (12), 4062–4075. https://doi.org/10.1021/acsbiomaterials.8b00916.

(5) Barabási, A.-L.; Stanley, H. E. Fractal Concepts in Surface Growth by A.- L. Barabási /core/books/fractal-concepts-in-surface-growth/0D9076FC287B60B2B1126BB165112F13 (accessed Sep 4, 2019). https://doi.org/10.1017/CBO9780511599798.

(6) Family, F.; Vicsek, T. Scaling of the Active Zone in the Eden Process on Percolation Networks and the Ballistic Deposition Model. *J. Phys. Math. Gen.* **1985**, *18* (2), L75–L81. https://doi.org/10.1088/0305-4470/18/2/005.

(7) Robbins, M. O.; Cieplak, M.; Ji, H.; Koiller, B.; Martys, N. Growth in Systems with Quenched Disorder. In *Growth Patterns in Physical Sciences and Biology*; Garcia-Ruiz, J. M., Louis, E., Meakin, P., Sander, L. M., Eds.; NATO ASI Series; Springer US: Boston, MA, 1993; pp 65–75. https://doi.org/10.1007/978-1-4615-2852-4_8.

(8) Puricelli, L.; Galluzzi, M.; Schulte, C.; Podestà, A.; Milani, P. Nanomechanical and Topographical Imaging of Living Cells by Atomic Force Microscopy with Colloidal Probes. *Rev. Sci. Instrum.* **2015**, *86* (3), 033705. https://doi.org/10.1063/1.4915896.